Redox Biology 57 (2022) 102474

Contents lists available at ScienceDirect

Redox Biology

journal homepage: www.elsevier.com/locate/redox

Mitochondrial oxidative stress contributes to diastolic dysfunction through impaired mitochondrial dynamics

Andrey Lozhkin [a], Aleksandr E. Vendrov [a], R. Ramos-Mondragón [b], Chandrika Canugovi [a], Mark D. Stevenson [a], Todd J. Herron [c], Scott L. Hummel [d,e], C Alberto Figueroa [f], Dawn E. Bowles [g], Lori L. Isom [b,h,i], Marschall S. Runge [a], Nageswara R. Madamanchi [a,*]

[a] 1150 West Medical Center Drive, 7200 Medical Science Research Building III, Department of Internal Medicine, Frankel Cardiovascular Center, University of Michigan, Ann Arbor, MI, 48019, USA
[b] Department of Pharmacology, University of Michigan, Ann Arbor, MI, USA
[c] Frankel Cardiovascular Regeneration Core Laboratory, Ann Arbor, MI, 48109, USA
[d] Department of Internal Medicine, Division of Cardiovascular Medicine, University of Michigan, Ann Arbor, MI, 48109, USA
[e] Ann Arbor Veterans Affairs Health System, Ann Arbor, MI, USA
[f] Department of Biomedical Engineering, University of Michigan, Ann Arbor, MI, USA
[g] Department of Surgery, Duke University School of Medicine, Durham, NC, USA
[h] Department of Neurology, University of Michigan, Ann Arbor, MI, USA
[i] Department of Molecular and Integrative Physiology, University of Michigan, Ann Arbor, MI, USA

ARTICLE INFO

Keywords:
Diastolic dysfunction
NADPH oxidase 4
NOX4 inhibitor
Cardiomyocyte
Heart failure with preserved ejection fraction
Mitochondrial dysfunction
Interstitial fibrosis

ABSTRACT

Diastolic dysfunction (DD) underlies heart failure with preserved ejection fraction (HFpEF), a clinical syndrome associated with aging that is becoming more prevalent. Despite extensive clinical studies, no effective treatment exists for HFpEF. Recent findings suggest that oxidative stress contributes to the pathophysiology of DD, but molecular mechanisms underpinning redox-sensitive cardiac remodeling in DD remain obscure. Using transgenic mice with mitochondria-targeted NOX4 overexpression (*Nox4*TG618) as a model, we demonstrate that NOX4-dependent mitochondrial oxidative stress induces DD in mice as measured by increased E/E′, isovolumic relaxation time, Tau Glantz and reduced dP/dt_{min} while EF is preserved. In *Nox4*TG618 mice, fragmentation of cardiomyocyte mitochondria, increased DRP1 phosphorylation, decreased expression of MFN2, and a higher percentage of apoptotic cells in the myocardium are associated with lower ATP-driven and maximal mitochondrial oxygen consumption rates, a decrease in respiratory reserve, and a decrease in citrate synthase and Complex I activities. Transgenic mice have an increased concentration of TGFβ and osteopontin in LV lysates, as well as MCP-1 in plasma, which correlates with a higher percentage of LV myocardial periostin- and ACTA2-positive cells compared with wild-type mice. Accordingly, the levels of ECM as measured by Picrosirius Red staining as well as interstitial deposition of collagen I are elevated in the myocardium of *Nox4*TG618 mice. The LV tissue of *Nox4*TG618 mice also exhibited increased I_{CaL} current, calpain 2 expression, and altered/disrupted Z-disc structure. As it pertains to human pathology, similar changes were found in samples of LV from patients with DD. Finally, treatment with GKT137831, a specific NOX1 and NOX4 inhibitor, or overexpression of m*CAT* attenuated myocardial fibrosis and prevented DD in the *Nox4*TG618 mice.

Together, our results indicate that mitochondrial oxidative stress contributes to DD by causing mitochondrial dysfunction, impaired mitochondrial dynamics, increased synthesis of pro-inflammatory and pro-fibrotic cytokines, activation of fibroblasts, and the accumulation of extracellular matrix, which leads to interstitial fibrosis and passive stiffness of the myocardium.

Further, mitochondrial oxidative stress increases cardiomyocyte Ca^{2+} influx, which worsens CM relaxation and raises the LV filling pressure in conjunction with structural proteolytic damage.

Abbreviations: Diastolic dysfunction, DD; NADPH oxidase 4, NOX4; hear failure with preserved ejection fraction, HFpEF.

* Corresponding author Department of Internal Medicine, University of Michigan, 7301A Medical Science Research Building III, 1150 W. Medical Center Dr, Ann Arbor, MI, 48109-5644, USA.
E-mail address: madamanc@med.umich.edu (N.R. Madamanchi).

https://doi.org/10.1016/j.redox.2022.102474
Received 16 August 2022; Accepted 11 September 2022
Available online 17 September 2022
2213-2317/© 2022 The Authors. Published by Elsevier B.V. This is an open access article under the CC BY-NC-ND license (http://creativecommons.org/licenses/by-nc-nd/4.0/).

1. Introduction

Heart failure (HF) is one of the leading cardiovascular diagnoses in the world with a high prevalence in older individuals. It is associated with poor quality of life and premature mortality. Approximately half of HF patients have preserved ejection fraction (HFpEF) [1] and the prevalence of HFpEF increases with age [2]. Despite normal left ventricular ejection fraction, HFpEF patients have high hospitalization and mortality rates, representing a significant public health burden [3]. In spite of several clinical trials over the past decades, there is currently no universal treatment strategy that improves outcomes and reduces mortality in HFpEF patients [4,5]. Recently, clinical trials of sodium-glucose cotransporter-2 (SGLT2) inhibitors have demonstrated promising results for reducing cardiovascular mortality or hospitalization in patients with HFpEF [6]. Nevertheless, HFpEF is a heterogeneous syndrome with multiple comorbidities that requires phenotype-specific therapy [4,5].

One of the early signs of HFpEF is reduced compliance of heart chambers due to increased passive stiffening of the myocardium [7]. Diastolic dysfunction (DD) is a major contributor to development of HFpEF [8], and it is characterized by impaired ventricular filling as a result of increased left ventricular (LV) stiffness, prolonged LV relaxation or both [9]. DD is identified in 66% of patients with HFpEF [10], and its prevalence increases with age [11].

Several studies indicate that oxidative stress may contribute to the pathophysiology of HF [12,13] and DD in both men and women [14,15]. Upregulation of mitochondria-localized NADPH oxidase 4 (NOX4), a constitutively active enzyme, is one of the main sources of reactive oxygen species (ROS) in aged hearts [16]. In addition, NOX4 has been identified as a major source of oxidative stress in mouse models of heart failure [17,18]. In mice fed a high fat diet, mitochondrial oxidative stress was associated with insulin resistance and diastolic dysfunction [19]. In previous studies we have shown that increased NOX4 expression in vascular smooth muscle cells (VSMC) following treatment with TGFβ increased expression of IL-6, MCP-1, RANTES and VCAM-1 [20]. Furthermore, mitochondria targeted overexpression of NOX4 results in increased aortic stiffness in mice [21], which plays a critical role in the development of HF and is associated with exercise intolerance in HFpEF [22].

Recently, impairment of mitochondrial function in the myocardium and peripheral muscle has been identified as an important contributor in the onset and progression of HFpEF [23]. Mouse studies found that Ang II treatment induced cardiac hypertrophy, DD, and hypertensive cardiomyopathy. Ang II-induced upregulation of NOX4 expression and oxidative damage to cardiomyocyte mitochondrial proteins lead to mismatch between ATP demand and production, which caused cardiac remodeling and inflammation [24]. A rat model of prediabetes has shown that impairment of cardiomyocytes caused by oxidative stress triggered DD before coronary endothelial dysfunction [25]. The mitochondrial quality control mechanism known as mitophagy is activated by mitochondrial dysfunction to remove damaged mitochondria [26]. Impairment of mitophagy exacerbated high fat diet-induced diabetic cardiomyopathy in mice [27].

Thus, studies suggest that pharmacologically reducing mitochondrial oxidative stress may be a beneficial strategy for improving mitochondrial function in DD and HFpEF. However, the precise molecular mechanisms underlying DD and HFpEF remain unknown in spite of the consensus that both mitochondrial malfunction and oxidative stress play a role. The question remains, however, whether oxidative stress and mitochondrial dysfunction are essential and sufficient for the development of left ventricular dysfunction. Therefore, in this study we tested the hypothesis that mitochondrial oxidative stress and dysfunction due to increased NOX4 expression/activity cause LVDD.

Using transgenic mice with mitochondria-targeted NOX4 overexpression, we demonstrated that increased H_2O_2 production causes mitochondrial dysfunction that leads to cardiomyocyte apoptosis. DD is caused by overexpression of pro-inflammatory and pro-fibrotic factors, the activation of fibroblasts, and excess accumulation of extracellular matrix.

2. Materials and methods

2.1. Animals

All animal procedures were performed in compliance with the protocols approved by the Institutional Animal Care and Use Committee of the University of Michigan in accordance with NIH OLAW policy. Wild-type mice were purchased from Jackson Laboratories (C57BL/6J; stock#000664). Both male and female mice were used at the age of 12 months. Animals were housed in specific pathogen free rooms, in ventilated cages at 22 °C with a 12 h light/dark cycle and free access to food and water. Mice were fed standard rodent chow diet.

Global transgenic mice with mitochondria-targeted overexpression of NOX4 (*Nox4*TG618) were generated as described [21]. Briefly, mitochondrial targeting sequence from the human cytochrome C oxidase gene, mouse *Nox4* coding sequence under CAG promoter and derivative of the pCx-EGFP plasmid were used to generate pCAG-Mito-*Nox4* transgene, which was microinjected into pronuclei of C57BL/6J embryos and implanted into pseudo-pregnant foster female mice. Breeding lines were established by crossing the founders with wild-type C57BL/6J mice. *Nox4* transgene-positive offspring identified by PCR using the primers:

5'-TTCGGCTTCTGGCGTGTGAC-3' and.

5'-AACATTTGGTGAATGTAGTAGTATTCTGGC-3'.

The mice with mitochondria-targeted human catalase (m*CAT)* were purchased from Jackson Laboratories (C57BL/6J background; stock #016197; 33) and were crossed with *Nox4*TG618 to generate double transgenic (*Nox4* x m*CAT*) mice.

For treatment with GKT137831 (Cayman Chemical), animals were randomly assigned to either drug or vehicle-receiving group. GKT137831 was dissolved in 0.5% carboxymethylcellulose, 0.25% Tween-20, and 1% DMSO and administered at a concentration of 60 mg/kg/day by oral gavage daily for 12 weeks starting at the age of 9 months. Both groups were housed together in the cages to avoid environmental bias.

2.2. Echocardiography

Mouse echocardiography analyses were done at the University of Michigan Physiology Phenotyping Core, supported by the Frankel Cardiovascular Center and the Department of Molecular and Integrative Physiology. Mice were anesthetized with 1–2% isoflurane/O_2 mixture to maintain a surgical plane of anesthesia and fixed on a ECG temperature-controlled board; body temperature was monitored with a rectal probe. Image acquisition and analysis were performed in a blinded manner. Echocardiography was performed with Visual Sonics' Vevo 2100 high resolution *in vivo* microimaging system with an MS-550D transducer with a center frequency of 40 MHz and a bandwidth of 22–55 MHz. Monitoring of electrocardiogram was done using noninvasive electrodes. Two-dimensional LV M-mode ultrasound images were acquired from long-axis and short-axis view. Pulsed wave Doppler and tissue Doppler imaging were also used to assess cardiac function.

The LV end-diastolic volume (LV EDV), fractional shortening (FS) and ejection fraction (EF) were measured with M-mode images taken in short-axis position at the papillary muscle level. Long-axis B-mode images were used to measure the left atrial volume (LA vol). An apical four chamber view pulse-wave Doppler tracing was used to measure mitral valve E velocity (MV E), mitral valve A velocity (MV A), and isovolumic relaxation time (IVRT).

2.3. Ventricular pressure-volume (PV) loop analysis

PV loop analysis was done at the University of Michigan Physiology

Phenotyping Core. Mice were anesthetized by inhalation of 1–1.5% isoflurane/O_2 mixture and were placed on a warming pad to maintain body temperature at 37 °C. A 1.4-F Scisense rodent pressure-volume catheter (Transonic; FTH-1212B-4518) was inserted into the left ventricle via an apical stab made with a 25-27-gauge needle. Pressure volume loops were collected at 1000 Hz, using ADVantage Pressure-Volume System ADV500 (Transonic). Left ventricular pressure-volume loops were recorded first at steady state and then after inferior vena cava occlusion. Data were analyzed with LabScribe v2 software (Iworx).

2.4. Mouse ventricular myocyte isolation

Mouse heart was cannulated through the aorta and perfused with a buffer containing 113 mM NaCl, 4.7 mM KCl, 0.6 mM KH_2PO_4, 0.6 mM Na_2HPO_4, 1.2 mM $MgSO_4$, 5.5 Mm $NaHCO_3$, 5.5 mM $KHCO_3$, 30 mM Taurine, 5.5 mM glucose, and 10 mM HEPES (pH 7.4) at 37 °C. After removal of blood, buffer containing collagenase type II and $CaCl_2$ (12 μM) was perfused for 10–12 min at 37 °C. Then, pulmonary veins and atrial tissue were removed from the heart and ventricles were gently minced followed by mechanical cellular dispersion with a plastic pipette. Isolated ventricular cardiomyocytes were transferred into a stopping solution (perfusion buffer with 10% fetal bovine serum) and calcium was reintroduced to a final concentration of 1.2 mM in 5 min intervals. Quiescent myocytes were used for patch clamping experiments.

2.5. L-type Ca^{2+} current recordings

Patch pipettes were prepared from borosilicate glass and the tip was fire-polished. Pipette resistance was 2.5–3.0 MΩ when contacted with the bath solution. After establishing the whole cell configuration, membrane capacitive components were eliminated using the features of the amplifier (Axon 700B; Digidata 1440) to avoid saturation. Electronic compensation (50–60%) was used to reduce the series resistance. Residual linear components were eliminated with a *–P/4* online subtraction protocol. L-type Ca^{2+} current (I_{CaL}) was recorded in whole cell configuration by applying repetitive 250 ms squared pulses ranging from −50 to 60 V from a holding potential of −50 mV. A pre-pulse of −30 from a holding potential of −80 mV was applied to inactivate sodium currents. The pipette solution contained 110 mM CsCl, 6 mM $MgCl_2$, 5 mM ATP, 4 mM tris-GTP, 10 mM HEPES and 15 mM TEA-Cl, pH 7.2. The bath solution contained 140 mM NaCl, 5.4 mM CsCl, 1.2 mM $CaCl_2$, 0.5 mM $MgCl_2$, 4 mM aminopyridine, 10 mM HEPES, pH 7.4. This solution was supplemented with 30 μM tetrodotoxin for blocking voltage-gated Na^+ channels (NaV channels). The voltage-dependence of activation was assessed by fitting current-voltage curves (I–V curves) to the following Boltzmann equation: ICa = Gmax (Vm-Vrev)/(1 + exp [(Vm-V1/2))/k]), where Gmax is the maximal conductance, Vm is the membrane potential, Vrev represents the apparent reversal potential, V1/2 is the membrane potential required to activate 50% of Gmax, and k is the slope factor.

2.6. Human samples

De-identified human left ventricular tissue samples were obtained from Duke Human Heart Repository, usage of the samples was approved by the University of Michigan Institutional Review Board. All samples were obtained from organ donors whose hearts were not used for transplantation and had a limited clinical history. All donors had normal LV sizes, and who did not have heart failure, with an EF higher than 45%. Among the samples, there were two groups: the control group (n = 3, age 51 ± 3 years, BMI 29.07 ± 6.17) and the group with documented history of moderate diastolic dysfunction (n = 3, age 52 ± 6.5 years, BMI 30.88 ± 5.84). Immediately after isolation, the heart samples were frozen in liquid nitrogen and stored at −80 °C. The frozen samples were used for protein isolation or embedded in OCT for cryosectioning.

2.7. Immunofluorescence staining

The mice were euthanized by inhaling isoflurane overdoses, the circulatory system was cleared by perfusion with 20 mL phosphate-buffered saline (PBS), LV tissues (N = 9) were collected and embedded in OCT (Fisher). Human and mouse LV tissue samples were cryosectioned at a thickness of 10 μm using a Leica CM3050 S cryostat (Leica Biosystems). Cryosections were fixed in acetone, permeabilized (for intracellular target labelling) with 0.1% Triton X100 and immunostained with rabbit anti-periostin (Sigma-Aldrich), rabbit anti-NOX4 (Abcam), rabbit anti-8-OHdG (Thermo Fischer Scientific), and rat anti-LAMP1 (Santa Cruz Biotechnology) antibodies. Alexa Fluor 595-conjugated goat anti-rabbit IgG (Invitrogen) was used as a secondary antibody. Fluorescently tagged antibodies used included Alexa Fluor 488-conjugated rabbit anti-myosin heavy chain (MYH), Alexa Fluor 488-conjugated rabbit anti-ATP5G2, Alexa Fluor 488-conjugated mouse anti-collagen I antibodies (Bioss), Cy3-conjugated mouse anti- α-smooth muscle actin antibody (ACTA2) (Sigma-Aldrich), and rhodamine-abeled wheat germ agglutinin (Vector Laboratories). The slides were washed in PBS and mounted in Vectashield HardSet antifade mounting medium with DAPI. All images were acquired with fluorescent microscope Nikon Microphot-FX (Nikon Instruments Inc) at the same exposure, gain, and offset. Single channel images were merged, and measures were performed using Fiji software (NIH).

The collagen I staining was determined by calculating the integrated density (mean gray value per area) within a defined region of interest (ROI) adjusted for the number of cell nuclei within the ROI. In LV cross sections with NOX4/MYH double-staining, integrated density of the double-positive signal was calculated and adjusted based on the number of cells within the ROI. LV cross sections were costained with 8-OHdG and ATP5G2, the integrated density of double-positive signal was determined, and the same procedure was performed for LAMP1/ATP5G2 co-staining. We counted periostin-positive or ACTA2-positive cells as a percentage of total cell number in images of human and murine LV cross sections stained with periostin/MYH and DAPI or ACTA2/MYH and DAPI.

2.8. MitoSOX red staining

For mitochondrial superoxide detection, human (N = 3) and mouse (N = 9) LV tissue sections were incubated with or without 5 μM MitoSOX (Invitrogen) Red at 37 °C for 15 min and fluorescence images were acquired immediately with Nikon Microphot-FX (Nikon Instruments Inc) microscope at the same exposure, gain, and offset. Control samples incubated in the presence of 200 U/mL PEG-SOD (Sigma) were used for background correction. Integrated density of the MitoSOX staining was determined using Fiji software (NIH).

2.9. MitoPY1 staining

For mitochondrial hydrogen peroxide detection, mouse LV tissue sections (N = 9) were incubated with 10 μM MitoPY1 (Sigma-Aldrich) in the presence and absence of 200 U/mL PEG-catalase (Sigma-Aldrich) for 60 min at 37 °C, then washed with DPBS and fluorescence images were acquired immediately with Nikon Microphot-FX (Nikon Instruments Inc) microscope at the same exposure, gain, and offset. The integrated density of MitoPY1 staining was calculated using Fiji software (NIH).

2.10. Annexin V staining

The percentage of pro-apoptotic cells in murine LV tissue was analyzed using the Annexin V Apoptosis Detection Kit (Invitrogen). Isolated ventricular cardiocytes were prepared as described in section 2.4. After washing with FACS buffer (PBS, 1% BSA, 1 mM EDTA), cells were stained with FITC-conjugated annexin V, and propidium iodide staining was performed to distinguish live from dead cells. The samples

were run on a Cytek Aurora spectral flow cytometer (Cytek), and the data were analyzed with FlowJo v10 (FlowJo).

2.11. Picrosirius red staining

Cryosections of human (N = 3) and mouse (N = 9) LV samples were air dried, fixed in 4% paraformaldehyde, and stained with Picrosirius Red Stain Kit (Abcam). Stained sections were washed in two changes of acidified water, dehydrated in three changes of 100% ethanol, and mounted in VectaMount permanent mounting medium (Vector Laboratories). Using a Nikon Microphot-FX microscopy in light microscopy mode, full-spectrum RGB images of stained myocardium were captured and analyzed using Fiji software (NIH). To assess fibrosis, we took five independent random images per sample. Hue, intensity, and saturation (HIS) characteristics of the images were used to establish two thresholds. A first threshold was used to count the area of the entire tissue; a second threshold was used to count areas stained in red. The percentage of Picrosirius Red-positive areas per given area of tissue was measured.

2.12. Single cell gel electrophoresis (comet assay)

Freshly isolated mouse LV tissue samples were lysed, and single cell suspensions were used in the assay. One thousand cells were resuspended into PBS and mixed with 1% melting agarose gel. The suspension was plated onto comet assay slides (Cell Biolabs) and left to solidify at room temperature without access to light. Next, the slides were immersed in ice-cold lysis buffer (1.2 M NaCl, 100 mM Na_2EDTA, 0.1% sodium lauroyl sarcosinate, 0.26 M NaOH, pH $>$ 13) for 1 h and then washed three times with ice-cold TBE buffer. Slides were then incubated in alkaline unwinding buffer for 1 h at 4°C. Later, slides with myocardial cells embedded in agarose were subjected to electrophoresis in alkaline running buffer for 30 min at 22 W, 4°C in the dark. Slides were stained with SYBR Gold nucleic acid gel stain (Invitrogen) and dehydrated with 100% ethanol. Images were made using fluorescent microscope Nikon Microphot-FX (Nikon Instruments Inc) at the same exposure, gain, and offset. The number of comets per area was counted. The data from an average of at least 15 areas per genotype was plotted.

2.13. Transmission electron microscopy

Transmission electron microscopy was done at the University of Michigan Microscopy Core. Freshly isolated samples of murine LV tissue were fixed in 3% glutaraldehyde +3% paraformaldehyde at 4 °C overnight. Later, the samples underwent post fixation treatment in 0.1 M carbonate-bicarbonate buffer and the secondary fixation was by 2% uranyl acetate, en block. Next, the samples were dehydrated in ethanol, with subsequent incubation in acetone. The samples were embedded in Spurr's Resin and sectioned with an ultramicrotome. Images were acquired using JEOL 3100R05 TEM (Jeol) and analyzed with Fiji software (NIH).

2.14. Western blot analysis

Human and mouse LV tissue samples were lysed in T-PER buffer (Thermo Fisher) supplemented with Halt Protease Inhibitor Cocktail (Thermo Scientific) using Qiagen Tissue Lyser II (Qiagen). Protein concentrations were determined using Pierce BCA protein assay kit (Thermo Fisher). Equal amounts of protein were loaded on 10% denaturing sodium dodecyl sulfate-polyacrylamide gels and subjected to electrophoresis, with subsequent transfer to a nitrocellulose membrane (GE Healthcare). Membranes were blocked with 1% BSA and incubated with primary antibodies, and then with a species-appropriate secondary anti-rabbit or anti-mouse fluorescently labelled IRDye secondary antibodies (Li-cor Biotechnology). Intensity of fluorescent signal was measured with Odyssey CLx imaging system (Li-cor Biotechnology) and analyzed using Fiji software (NIH). The following primary antibodies were used: rabbit anti-phospho-DRP1, rabbit anti-DRP1, rabbit anti-mitofusin-1, rabbit anti-mitofusin-2, rabbit anti-OPA1, rabbit anti-VDAC, rabbit anti-calpastatin, rabbit anti-calpain 1, rabbit anti-calpain 2, rabbit anti-OPA1 (Cell Signaling Technology), mouse anti-LC3α/β, mouse anti-parkin, mouse anti-PINK1, mouse anti-FIS1 (Santa Cruz Biotechnology), rabbit anti-NOX4 antibody (Abcam), and mouse anti-β-tubulin (Sigma-Aldrich).

2.15. ELISA

Concentrations of MCP-1, osteopontin, and TGFβ in protein lysates were measured using Osteopontin (OPN/SPP1) Mouse ELISA Kit, MCP-1 Mouse ELISA Kit (Thermo-Fisher), and Mouse TGF beta 1 ELISA Kit (Abcam), respectively. Measurements were made according to the manufacturer's instructions. Absorbance was measured at 450 nm on SpectraMax iD5 multi-mode microplate reader (Molecular Devices).

2.16. Mitochondrial DNA damage and copy number assays

Genomic DNA was extracted from murine LV tissue using the DNAeasy Blood and Tissue Kit (Qiagen). Concentrations of DNA were measured with Nano-Drop ND-1000 spectrophotometer and Quant-iT PicoGreen dsDNA Assay Kit (Thermo-Fisher). Long mitochondrial DNA fragment was amplified using LongAmp™ Taq PCR kit (New England biolabs) as per manufacturers protocol. A 10-kb- mitochondrial fragment was amplified using 500 ngs of genomic DNA per 50 μl reaction volume with forward primer: GCCAGCCTGACC CATAGCCATAATAT and reverse primer: GAGAGATTTTATGGGTGTAATGCGG, and an 8.7 kb β-globin gene fragment was amplified using forward primer TTGAGACTGTGATTGCGAATGCCT and reverse primer CCTTTAATGCCCATCCCGGCAT. The yield of long-range PCR was measured with Quant-iT PicoGreen dsDNA (Thermo-Fisher) Assay Kit. We subjected the long-range PCR product to electrophoresis on a 0.5% agarose gel to identify the size of band and then quantified the band intensity. The DNA yield was quantified by PicoGreen assay. Relative amplification of mitochondrial fragment was normalized to input DNA and relative mitochondrial copy number. Relative mitochondrial copy number was measured by a short fragment amplification using MTCO1-specific Taqman probe normalized to a short fragment amplification of nuclear GAPDH specific Taqman probe (Applied biosystems).

2.17. Seahorse assay

We used Seahorse XFe96 analyzer (Agilent Technologies) to quantify cardiomyocyte mitochondrial bioenergetics. Five thousand ventricular cardiomyocytes per well were plated in a Seahorse XFe96 Spheroid Microplates (Agilent technologies). Seeding medium was replaced with unbuffered Seahorse XF DMEM assay medium (Agilent technologies) containing 25 mM glucose and 1 mM sodium pyruvate 60 min prior to the assay and the cells incubation continued in a CO_2 free conditions. Analysis was performed using Seahorse XF Cell Mito Stress Test Kit (Agilent Technologies). After measuring basal oxygen consumption rate (OCR) and extracellular acidification rate (ECAR), the following compounds were automatically injected: 2 μM oligomycin, an inhibitor of ATP synthase; 1 μM carbonyl cyanide p-[trifluoromethoxy]-phenylhydrazone (FCCP), a chemical proton ionophore that uncouples the oxygen consumption from ATP synthesis; 0.5 μM rotenone + 0.5 μM antimycin A, inhibitors of mitochondrial electron transport chain complex I and III, respectively. Basal mitochondrial respiration, ATP-driven OCR, maximal cellular respiration, reserve capacity and non-mitochondrial oxygen consumption were calculated.

2.18. Complex I activity

Mitochondrial ETC (electron transport chain) complex I activity was detected with Complex I Enzyme Activity Assay Kit (Abcam) according

to manufacturer's protocol. Fresh LV tissue was harvested, homogenized in PBS using Qiagen Tissue Lyser II (Qiagen), and protein was extracted using detergent solution provided with the kit. Protein concentrations were determined using Pierce BCA protein assay kit and was adjusted to 5 mg/mL. Linear rate of increase in absorbance at OD 450 nm was determined with SpectraMax iD5 multi-mode microplate reader.

2.19. Citrate synthase activity

Citrate synthase activity was assessed with MitoCheck® Citrate Synthase Activity Assay Kit (Cayman Chemical) according to manufacturer's instruction. Fresh mouse and frozen human LV tissue samples were homogenized in T-PER buffer (Thermo Fisher) supplemented with Halt Protease Inhibitor Cocktail (Thermo Scientific) using Qiagen Tissue Lyser II (Qiagen), and protein concentrations determined using Pierce BCA protein assay kit. Samples were incubated with oxaloacetate, Acetyl Co-A and developing reagent. Production of tricarboxylate citrate was assessed by absorbance at 412 nm every 30 s at 25 °C in SpectraMax iD5 multi-mode microplate reader.

2.20. Amplex Red assay

Generation of H_2O_2 in mouse LV tissue was determined with Amplex Red hydrogen peroxide/peroxidase assay kit (Invitrogen) according to manufacturer's protocol. Briefly fresh frozen tissue (30 mg) was incubated with Amplex Red reagent/HRP solution (100 μM Amplex Red, 1 U/mL horseradish peroxidase) in Krebs-HEPES buffer for 30 min in the dark. SpectraMax iD5 multi-mode microplate reader with excitation at 530 nm and fluorescence emission detection at 590 nm was used to analyze the fluorescent signal, and values derived from the no-H_2O_2 control were subtracted and calculations were made based on H_2O_2 standard curve. H_2O_2 measurements were normalized to dry tissue weight.

2.21. Statistical analyses

All statistical analyses were performed using Prism 9 software (GraphPad), and data sets were tested for normality with Kolmogorov-Smirnov test. All data were presented as mean ± SEM. A comparison between groups was performed using unpaired *t*-test or one-way ANOVA followed by Newman-Keuls multiple comparisons test. Two-way ANOVA was used to test for the effect of interaction between genotype and age on H_2O_2 production in Amplex Red analysis. A value of $P < 0.05$ was considered significant.

3. Results

3.1. Diastolic dysfunction is associated with increased expression of mitochondrial NOX4 and oxidative stress in human LV myocardium

Increased NOX4 expression and activity are a major source of oxidative stress in failing heart [17,18]. It is well established that NOX4 localizes to mitochondria in several cell types, including cardiomyocytes, and it is an important contributor to mitochondrial oxidative stress [17,28,29]. To determine whether mitochondrial NOX4 expression was increased in DD, a precursor to diastolic heart failure [30], we compared NOX4 expression in LV myocardium samples from patients with DD and a healthy control group. Western blot analysis of heart protein lysates revealed a 3.2-fold higher expression levels of NOX4 in the DD group compared to control ($P < 0.01$; Fig. 1A). Consistent with this result, immunofluorescence analysis of NOX4 expression in LV cryosections showed significantly higher levels of the oxidase in cardiomyocytes of the DD group ($P < 0.05$; Fig. 1B).

To determine the functional significance of increased mitochondrial

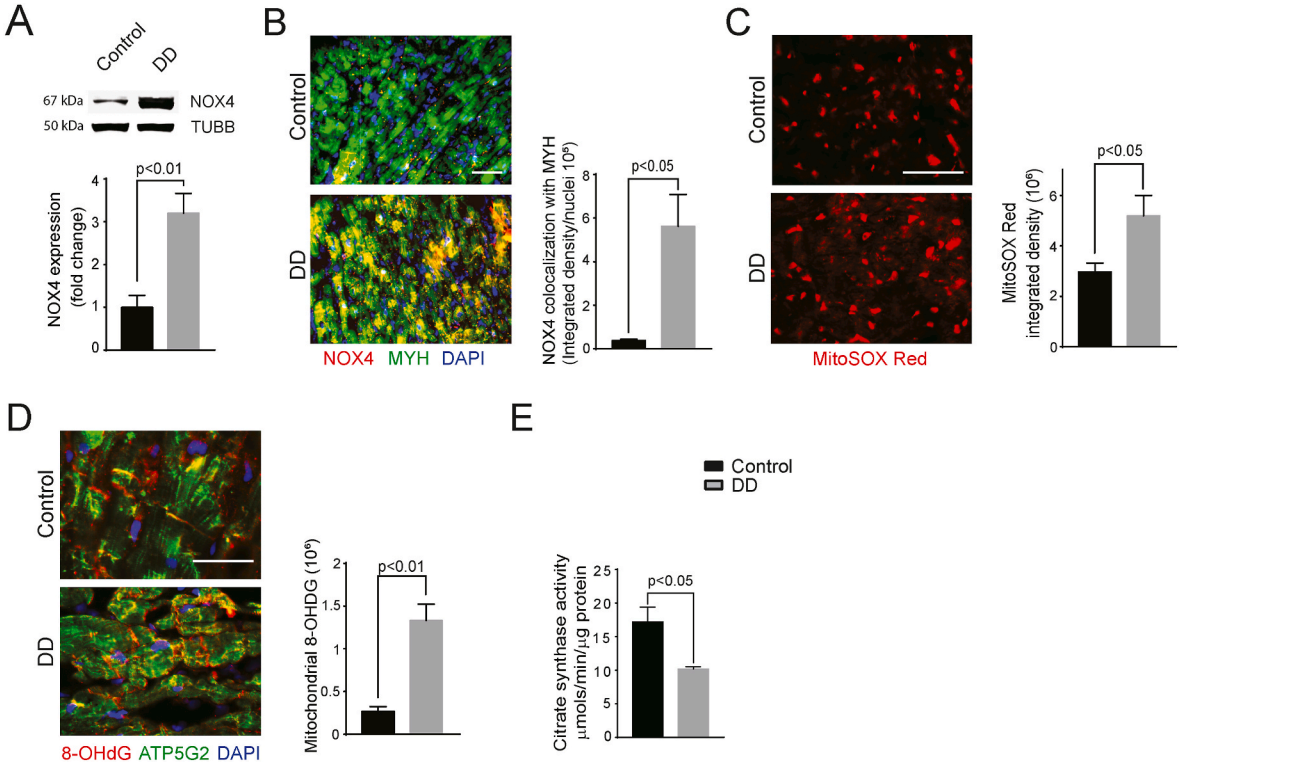

Fig. 1. Increased expression of NOX4 is associated with mitochondrial oxidative stress and dysfunction in LV myocardial samples from patients with a history of diastolic dysfunction.
(A) Representative Western Blot analysis and quantification of NOX4 expression in human LV myocardial samples. **(B)** Representative immunofluorescence images and quantifications of NOX4. **(C)** MitoSOX and **(D)** ATP5G2/8-OHDG staining in human LV myocardial cross sections. **(E)** Citrate synthase activity was measured in protein lysates of LV myocardium. The data are presented as mean ± SEM, N = 3. Scale is 100 μm.

NOX4 levels in DD cardiomyocytes, we measured mitochondrial superoxide levels in patient myocardial cross sections. MitoSOX red fluorescence in DD samples was significantly higher than in control samples (3-fold, $P < 0.05$; Fig. 1C). Concordantly, co-localization of the oxidative DNA damage marker 8-OHdG with mitochondrial marker ATP5G2 in LV cross sections of DD group was significantly higher than control ($P < 0.01$; Fig. 1D), indicating greater myocardial mtDNA damage. Citrate synthase activity, a marker of mitochondrial content and oxidative capacity [31], was lower in the LV protein lysates of the DD group versus the control subjects ($P < 0.05$; Fig. 1E), suggesting a combination of reduced mitochondrial volume and impaired mitochondrial function. Together, these data suggest that increased expression and activity of cardiomyocyte NOX4 increases mitochondrial oxidative stress and dysfunction, contributing to the pathogenesis of DD.

3.2. *Nox4TG618 mice show diastolic dysfunction*

Myocardial mitochondrial NOX4 levels increase with aging and stress [16], and cardiac-specific overexpression of *Nox4* in mice induces aging-associated cardiac phenotypes, including left ventricular dysfunction, apoptosis, and fibrosis [32]. We demonstrated that young *Nox4*TG618 mice with elevated mitochondrial NOX4 phenocopy aging-associated aortic stiffening [21], an independent risk factor for DD. Since our human data indicated that increased cardiomyocyte NOX4 expression and activity may contribute to the pathogenesis of DD, we used pulsed-wave and tissue Doppler echocardiography to study left

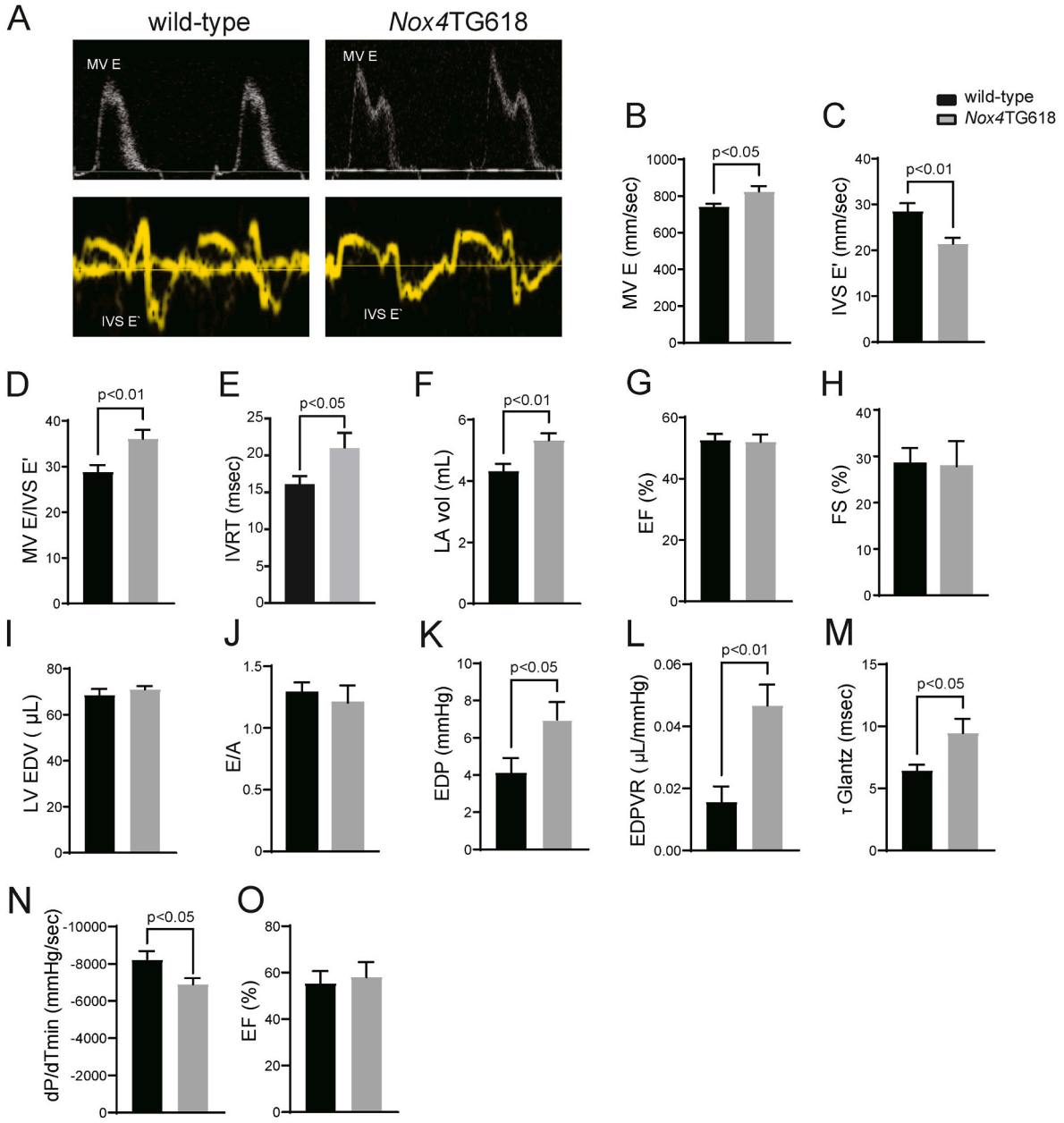

Fig. 2. Increased mitochondrial NOX4 expression leads to cardiac diastolic dysfunction in *Nox4*TG618 mice.
Systolic and diastolic function parameters in wild-type and *Nox4*TG618 mice **(A–G)** were assessed by echocardiography. **(A)** Representative pulsed wave and tissue Doppler images. **(B)** Mitral valve (MV) E velocity (MV E), **(C)** MV septal annulus velocity E′ (E′), **(D)** ratio of MV E velocity to E′ velocity at septal annulus (E/E′), **(E)** isovolumic relaxation time (IVRT), **(F)** left atrial volume (LA vol), **(G)** ejection fraction (EF), **(H)** fractional shortening, **(I)** LV end-diastolic volume (LV EDV), and **(J)** mitral valve E to A ratio (N = 15). Pressure-volume loops analysis **(K–O)**. **(K)** end-diastolic pressure (EDP), **(L)** end diastolic pressure volume relationship (EDPVR), **(M)** Tau Glantz (T Glantz), **(N)** rate of ventricular pressure decrease (dP/dT_{min}), and **(O)** ejection fraction (EF); (N = 7). The data presented as mean ± SEM.

ventricle function in middle aged (12-month-old) *Nox4*TG618 and wild-type mice (Fig. 2A–J). There was a significant elevation in mitral valve E velocity (MV E, $P < 0.05$; Fig. 2B), a decreased mitral valve septal annulus velocity E′ (IVS E′, $P < 0.05$; Fig. 2C) and a higher E/E′ ratio ($P < 0.01$; Fig. 2D) in *Nox4*TG618 mice compared with the wild-type mice. Transgenic animals also displayed elevated isovolumic relaxation time (IVRT) ($P < 0.05$; Fig. 2E), suggesting impaired diastolic function. Additionally, transgenic mice showed an increase in left atrial volume ($P < 0.01$, Fig. 2F), indicative of an elevated LV filling pressure. However, there were no significant differences in ejection fraction and fractional shortening, LV end diastolic volume and E/A (Fig. 2G–J).

Because of the limited sensitivity of echocardiography for detecting elevated LV filling pressure, we also performed pressure-volume loop analysis for a comprehensive assessment of cardiac systolic and diastolic

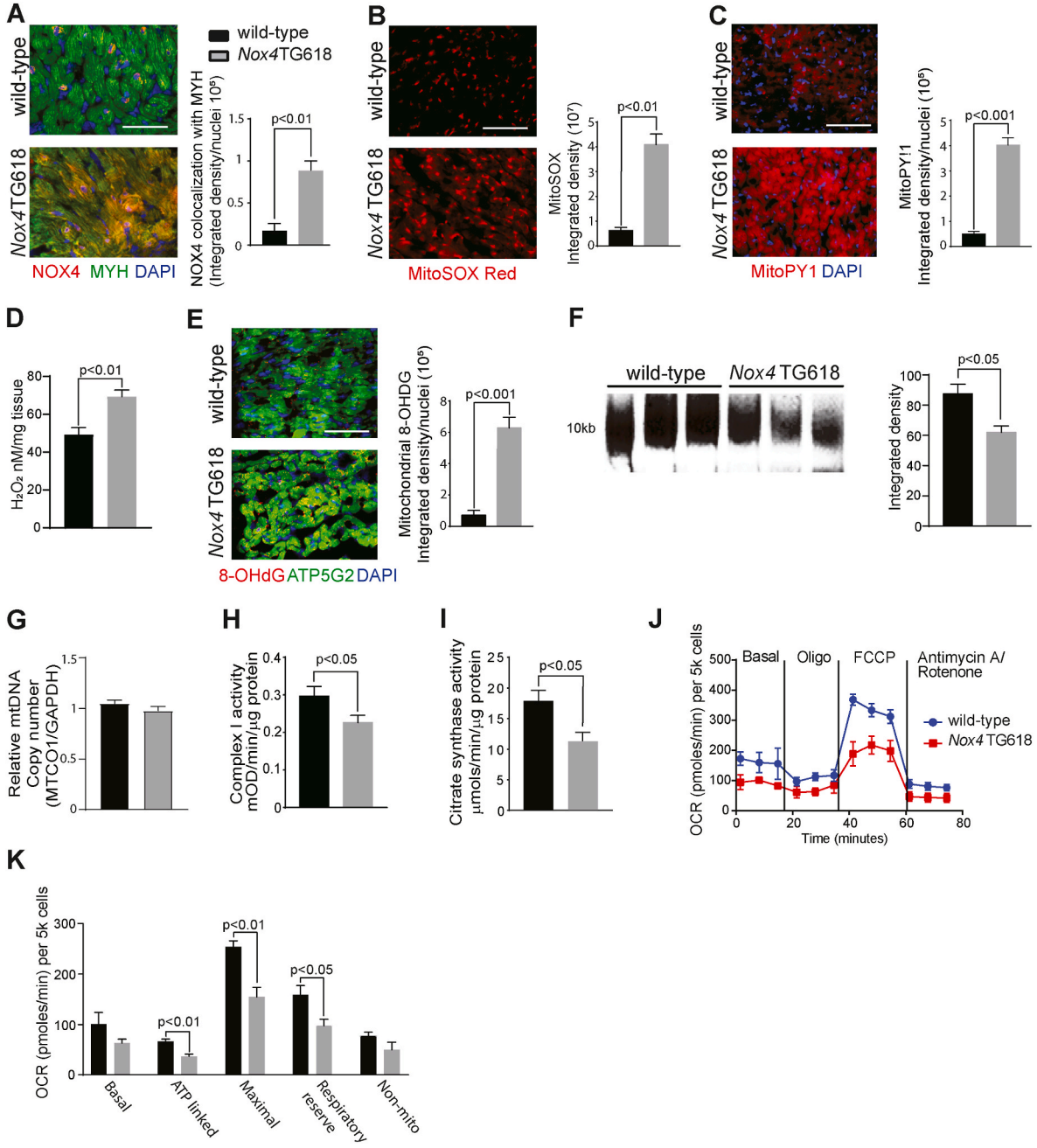

Fig. 3. Increased mitochondrial NOX4 expression in mice increases mitochondrial oxidative stress, mtDNA damage, and leads to mitochondrial dysfunction in LV cardiomyocytes.

Representative immunofluorescence images and quantification of LV cross sections from wild-type and *Nox4*TG618 mice stained for **(A)** NOX4 and counterstained with cardiomyocyte marker MYH, **(B)** MitoSOX Red, and **(C)** MitoPY1, (N = 9). **(D)** Mouse LV H_2O_2 levels were measured by Amplex Red assay (N = 7). **(E)** ATP5G2/8-OHdG colocalization, (N = 9). **(F)** Representative long PCR amplicon showing amplification of 10 kb mitochondrial DNA in mouse LV samples. The amplified mitochondrial DNA band was normalized to a short PCR amplicon of 0.22 kb and the band intensity was quantified by densitometry. **(G)** Data represent relative mitochondrial DNA copy number in LV tissues of wild-type and transgenic mice (N = 4). **(H)** Citrate synthase activity was measured in mouse LV lysates (N = 10). **(I)** Complex I activity measured in mouse LV lysates (N = 10). **(J)** Mitochondrial oxygen consumption rate (OCR) measured by Seahorse analysis (N = 5). **(K)** Mitochondrial bioenergetics parameters derived from OCR, (N = 5). The data are presented as mean ± SEM. Scale is 100 μm. . (For interpretation of the references to colour in this figure legend, the reader is referred to the Web version of this article.)

function (Fig. 2K-O) [33]. The increased end-diastolic pressure (EDP, $P < 0.05$; Fig. 2K) and elevated end-diastolic pressure-volume relationship (EDPVR, $P < 0.01$; Fig. 2L) in *Nox4*TG618 animals is consistent with an increase in LV diastolic myocardial stiffness and increased filling pressure compared with wild-type, which is in consonance with echocardiography results. Two independent indices of left ventricle relaxation are the isovolumic relaxation constant (Tau Glantz) and minimum rate of pressure change (dP/dtmin). The increased Tau Glantz ($P < 0.05$; Fig. 2M) suggests prolonged relaxation time of the LV, and the reduced dP/dt_{min} ($P < 0.05$; Fig. 2N) indicates prolonged isovolumic relaxation time of the LV in transgenic mice. The ejection fraction of transgenic animals was preserved in accordance with echocardiography data (Fig. 2O). There were no significant differences in body weight, mean blood pressure, and heart rate between wild-type and *Nox4*TG618 mice (SI Appendix, Fig. S1 A-C). Similarly, plasma creatinine, blood urea nitrogen (BUN), alanine transaminase (ALT), aspartate aminotransferase (AST), albumin (ALB), and total bilirubin levels were not different between wild-type and transgenic mice (SI Appendix, Fig. S1 D-I). *Nox4*TG618 mice showed no abnormalities in kidney or liver histology after H&E staining (SI Appendix, Fig. S1 J, K). Together, LV pressure-volume loop analyses and echocardiography analyses confirm the presence of DD without a change in global systolic function in *Nox4*TG618 mice.

3.3. The diastolic dysfunction in Nox4TG618 mice is associated with myocardial mitochondrial oxidative stress and mtDNA damage, as well as cardiomyocyte mitochondrial dysfunction

We have previously shown increased global *Nox4* expression in *Nox4*TG618 mice [21]. Compared to wild-type mice, NOX4 protein levels are four times higher in the ventricular cardiomyocytes of transgenic mice, as reflected by the increased yellow fluorescence resulting from colocalization of immunoreactive NOX4 and cardiomyocyte marker MYH in ventricular sections ($P < 0.01$, Fig. 3A). Consequently, MitoSOX Red fluorescence in LV cross sections revealed elevated myocardial mitochondrial superoxide production in *Nox4*TG618 mice ($P < 0.01$; Fig. 3B). The transgenic mice also showed a significant increase in mitochondrial and total cellular H_2O_2 levels in the LV ($P < 0.001$ and 0.01; Fig. 3C and D, respectively). In agreement with the report that mitochondrial ROS and mtDNA damage contribute to the development and progression of LV remodeling and failure [34], myocardial mtDNA damage was increased in transgenic mice, as shown by increased yellow fluorescence from colocalization of immunoreactive nonnuclear 8-OHdG and ATPG52 (ATP synthase 5 subunit 2, a mitochondrial marker) in LV cross sections ($P < 0.001$; Fig. 3E). Accordingly, a 40% decrease in long PCR amplification of 10 kb mtDNA from *Nox4*TG618 LV myocardial samples was found compared with the wild-type mice ($P < 0.05$; Fig. 3F), while relative mtDNA copy number was not different between the genotypes (Fig. 3G). These data suggest that mitochondrial DNA copy number does not directly correlate with mtDNA damage [35] and that mitochondrial biogenesis, fission, and fusion may adjust for any potential loss in mtDNA copy number [36].

We reported previously that increased mitochondrial NOX4 expression/activity in aging reduces mitochondrial oxidative capacity in vascular cells [28]. We and others have also shown that mtDNA damage lowers mitochondrial respiration and increases CVD susceptibility [21,29,37]. Complex I and citrate synthase and activities in LV lysates from Nox4TG618 mice were significantly lower than in wild-type samples ($P < 0.05$; Fig. 3H and I). Supporting these findings, ventricular cardiomyocytes from middle-aged *Nox4*TG618 mice showed a significant decrease in ATP-driven ($P < 0.01$) and maximal mitochondrial oxygen consumption rate (OCR; $P < 0.01$). Furthermore, bioenergetic analysis revealed considerable decreases in reserve respiratory capacity ($P < 0.05$; Fig. 3J and K). Together, the results of these studies demonstrate that mitochondrial oxidative stress, mtDNA damage and decreased mitochondrial function in ventricular cardiomyocytes cause DD in *Nox4*TG618 mice.

3.4. Nox4TG618 mice exhibit impaired myocardial mitochondrial dynamics and cardiomyocyte apoptosis

Because increased NOX4 levels are associated with impaired mitochondrial bioenergetics [21,28], we examined mitochondrial dynamics and turnover in the cardiomyocytes of *Nox4*TG618 mice. A transmission electron microscopy (TEM) analysis of mouse heart sections showed a large number of small and fragmented mitochondria with a significant reduction in size (3-fold, $P < 0.0001$; Fig. 4A) in *Nox4*TG618 cardiomyocytes compared with wild-type. The expression level of VDAC, a mitochondrial outer membrane protein, was not different between wild-type and *Nox4*TG618 ventricular lysates (Fig. 4B), suggesting that cellular mitochondrial volume density is not affected in the ventricles of transgenic mice.

The dynamic morphology of mitochondria is determined by the antagonistic effects of mitochondrial fission and fusion, also known as mitochondrial dynamics, as well as their movement along cytoskeletal tracks [38]. A variety of GTPases regulate mitochondrial fission and fusion: MFN1 and MFN2 promote fusion of the outer mitochondrial membrane, while optic atrophy protein 1 (OPA1) promotes fusion of the inner mitochondrial membrane [39]. Mitochondrial fission is regulated by dynamin-related protein 1 (DRP1) and fission protein 1 (FIS1). Fission and fusion ensure mitochondrial quality control by separating functional and dysfunctional fragments of mitochondria and fusion of the functional mitochondria [40]. To examine the potential effects of mitochondrial oxidative stress and dysfunction on mitochondrial dynamics, we measured the expression of mitochondrial fission and fusion proteins and mitophagy in ventricular lysates from wild-type and *Nox4*TG618 mice (Fig. 4B). The expression of FIS1 and DRP1 in LV myocardial extracts did not differ between genotypes. However, DRP1 Ser 616 phosphorylation was significantly increased ($P < 0.05$) in *Nox4*TG618 mice compared to wild-type, indicating increased activation. These findings suggest that mitochondrial fission is enhanced in the cardiomyocytes of transgenic mice, and that this result correlates with reduced mitochondrial size as assessed by TEM. While the expression levels of OPA1 and MFN1 did not differ between genotypes, the expression of MFN2 was markedly reduced in *Nox4*TG618 mice ($P < 0.05$; Fig. 4C), indicating that mitochondrial fusion defects also contribute to mitochondrial size reduction.

Following fission, dysfunctional mitochondria undergo lysosomal degradation via mitophagy [39]. Therefore, we examined the expression of proteins involved in mitophagy pathway activation. We found no genotypic expression of PINK1, PARKIN or MAP1LC3B in LV protein lysates (Fig. 4D). Further, immunofluorescence colocalization of the lysosomal marker LAMP1 with mitochondrial marker ATP5G2 was not different between genotypes (Fig. 4E), suggesting no differences in mitophagy flux. These results suggest that mitochondrial size loss is likely related to increased mitochondrial fission and decreased fusion without changes in mitophagy, indicating impaired mitochondrial turnover in *Nox4*TG618 mice.

Emerging evidence indicates an intense crosstalk between the mitochondrial dynamics and apoptosis [40]. Fission is an early event during apoptosis, and DRP1 is known to increase the release of cytochrome *c* during apoptosis [41]. Therefore, we compared nuclear DNA damage and cardiomyocyte apoptosis in ventricular sections between wild-type and *Nox4*TG618 mice. The number of ventricular cardiomyocytes with comet tails was significantly higher (3.7-fold, $P < 0.001$; Fig. 4F) in *Nox4*TG618 than in wild-type mice. An Annexin V flow cytometry assay detected significantly more apoptotic cells in cardiomyocyte-enriched ventricular cell suspensions of transgenic animals (0.48% in wild-type versus 4.75% in *Nox4*TG618, $P < 0.01$; Fig. 4G). In summary, our data show that mitochondrial oxidative stress caused by increased expression of NOX4 causes mitochondrial dysfunction, impairs mitochondrial dynamics and exacerbates nuclear

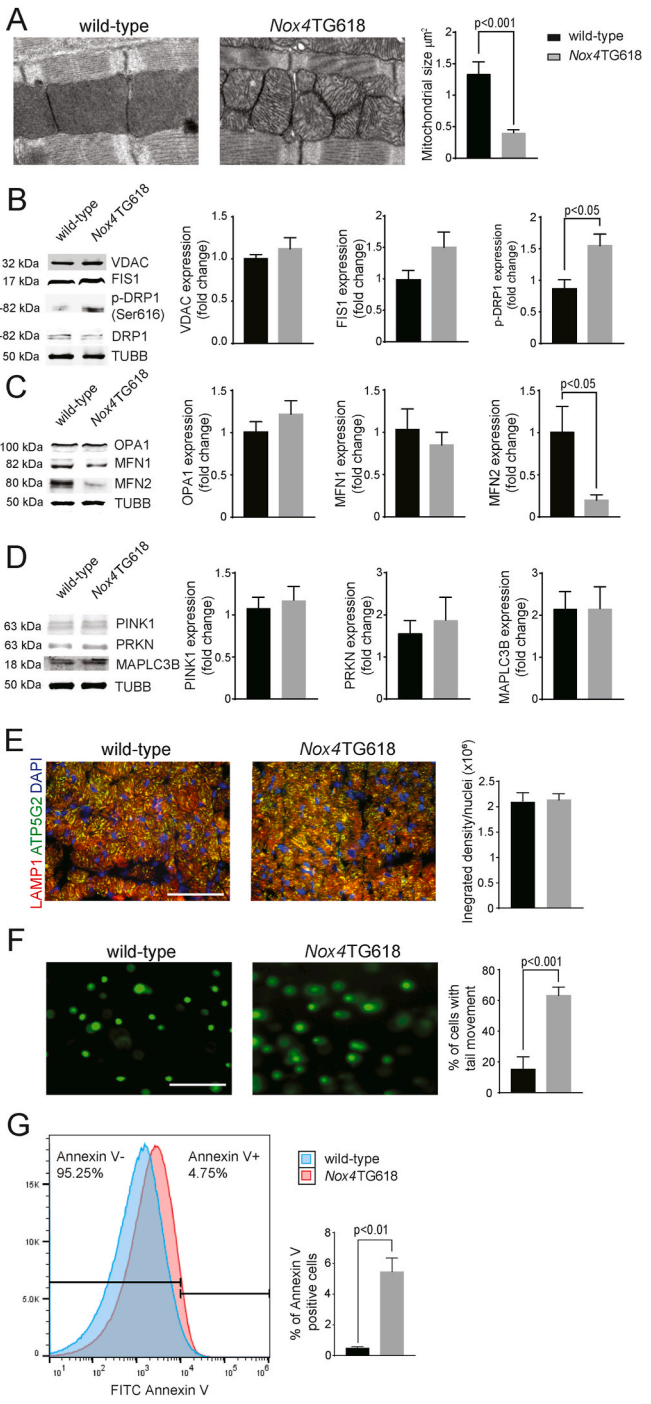

Fig. 4. Mitochondrial dynamics are impaired in the left ventricle of *Nox4*TG618 versus wild-type mice.
(A) Representative TEM images and quantification of mitochondrial size in mouse LV cross sections (N = 3). Representative Western blot analysis and quantification of proteins involved in mitochondrial fission **(B)**, fusion **(C)** and mitophagy **(D)**; (N = 4). **(E)** Representative immunofluorescent images and quantification of mouse LV sections stained with LAMP1/ATP5G2, (N = 9). **(F)** Representative comet assay images of cardiomyocytes isolated from LV samples and quantification of comet tails in *Nox4*TG618 versus wild-type mice (N = 3). **(G)** Flow cytometric analysis of LV cardiomyocyte apoptosis, % of cells positive for Annexin V (N = 5). Data presented as mean ± SEM. Scale is 100 µm.

DNA damage and apoptosis in the hearts of transgenic animals.

3.5. *L-type Ca^{2+} current and calpain 2 expression are increased in ventricular cardiomyocytes of Nox4TG618 mice*

Proper Ca^{2+} handling is important for normal cardiomyocyte function [40]. Calcium channel blockers improve diastolic function by lowering cytoplasmic Ca^{2+} concentrations and relaxing cardiomyocytes [43]. Ca^{2+} influx through L-type calcium channels (LTCCs) is the main source of intracellular Ca^{2+} in the myocytes [34].

Activation of the L-type Ca^{2+} current (I_{CaL}) increases intracellular Ca^{2+} concentration, which promotes mitochondrial uptake, resulting in elevated production of mtROS, which in turn leads to sustained I_{CaL} activation [44]. To investigate a possible activation of the I_{CaL} by mtROS, we performed whole-cell patch clamp recordings from acutely isolated ventricular cardiomyocytes from *Nox4*TG618 and wild-type mice (Fig. 5A). The density of I_{CaL} in *Nox4*TG618 was higher than in wild-type myocytes. On the 10 mV peak of the IV curves, the *Nox4*TG618 myocytes had an I_{CaL} density of -8.1 ± 0.5 pA/pF in comparison to -7.0 pA/pF in the wild-type myocytes ($P < 0.05$; Fig. 5B). Conductance measurements from I–V relationships revealed that the Nox4TG618 cardiomyocytes had higher degree of activation of the LTCCs than wild-type cardiomyocytes were more active in the compared to wild-type cardiomyocytes (Fig. 5C). Normalizing activation curves by maximum conductance Gmax however did not reveal any changes in voltage-dependent LTCC activation (Fig. 5D). The membrane capacitance (Fig. 5E) and the heart weight normalized by the tibia length did not differ between genotypes (Fig. 5F), suggesting that the increased I_{CaL} density was not caused by cardiomyocyte hypertrophy in transgenic animals.

The calpains are Ca^{2+}-dependent proteases. Recent evidence has suggested that LTCC activity is required for the activation of calpains [45]. We used Western blot analysis to determine the expression of components of the calpain system. The protein levels of calpain 1 and its inhibitor calpastatin were similar in ventricular myocardium lysates from transgenic and wild-type mice (Fig. 5G). In contrast, calpain 2 protein expression was significantly upregulated in Nox*4*TG618 (4.9-fold, $P < 0.001$; Fig. 5G). Congruent with this, we observed Z-line streaming and sarcomere disarrangement on TEM images of *Nox4*TG618 heart sections (Fig. 5H). However, there was no difference in titin N2BA/N2B ratio (SI Appendix, Fig. S2) in LV lysates between genotypes, indicating that titin expression diffrences are unlikely to affect LV passive stiffness. These data suggest that upregulation of the LTCC activity caused by high mtROS may be an upstream modulator of the calpain 2 activity and Z-disc damage in *Nox4*TG618 cardiomyocytes.

3.6. *Nox4TG618 mice develop myocardial fibrosis*

Passive myocardial stiffness contributes to DD and is often found in the heart tissues of patients with HFpEF [46]. Myocardial interstitial fibrosis is a significant factor contributing to passive stiffening [47]. Picrosirius red staining of ventricular cross sections from *Nox4*TG618 mice revealed significantly more positively stained areas than those in wild-type mice ($P < 0.001$; Fig. 6A). Consistent with this result, interstitial collagen I levels were significantly higher ($P < 0.0001$; Fig. 6B). An analysis of periostin staining of heart sections using immunofluorescence microscopy revealed a higher number of activated fibroblasts in *Nox4*TG618 hearts ($P < 0.001$; Fig. 6C). Transgenic mice also showed increased presence of myofibroblasts indicated by increased ACTA2 staining ($P < 0.0001$, Fig. 6D) and absence of desmin staining (data not shown). There were no differences in cardiomyocyte cross-sectional area between genotypes, indicating the absence of cardiac hypertrophy (Fig. 6E). In accordance with increased myocardial fibrosis, there was a significant increase in the levels of pro-fibrotic factor TGFβ ($P < 0.0001$; Fig. 6F) in *Nox4*TG618 LV lysates ($P < 0.0001$; Fig. 6F).

Similarly, *Nox4*TG618 LV lysates showed higher expression of

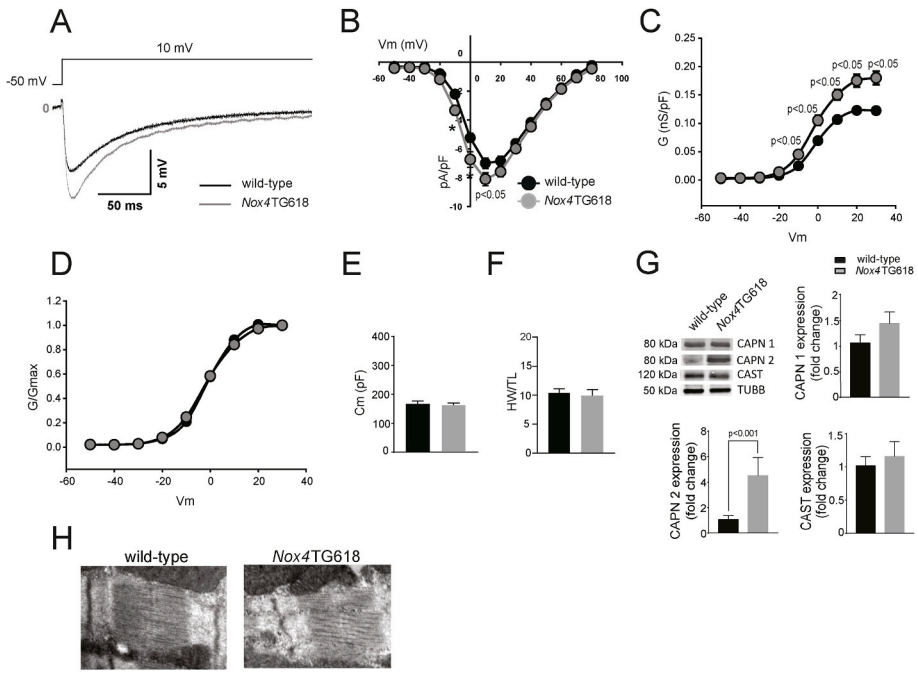

Fig. 5. Increased mitochondrial NOX4 expression in *Nox4*TG618 mice is associated with upregulated L-type Ca^{2+} current (I_{CaL}), increased expression of calpain 2 and fractured sarcomeric Z-discs in cardiomyocytes.
(A) Representative recordings of the I_{CaL} in wild-type and *Nox4*TG618 mice elicited at 10 mV, **(B)** voltage-current curves (Vm), **(C)** conductance (G), **(D)** normalized conductance (G/Gmax), and **(E)** membrane capacitance. For I_{CaL} recordings, cardiomyocytes (n = 27 wild-type and 30 *Nox4*TG618) from 4 mice of each genotype were used. **(F)** A normalized weight for the heart based on the length of the tibia; (N = 4). **(G)** Representative Western blot analysis and quantification of expression of calpain1/2 (CAPN1/2) and calpastatin (CAST) (N = 6) in LV lysates. **(H)** Representative TEM images of murine LV cross sections with focus on Z-disc (N = 3). The data are presented as mean ± SEM.

osteopontin, a matricellular

Protein implicated in monocytes/macrophages recruitment and the regulation of cytokine production in innate immune cells [48] ($P < 0.05$; Fig. 6G). Moreover, the levels of MCP-1, a chemokine involved in macrophage recruitment, were higher in the plasma of transgenic mice than in the plasma of wild-type mice ($P < 0.05$; Fig. 6H) [49]. Together, these data suggest that in *Nox4*TG618 mice cardiomyocyte damage associated with mitochondrial OS and dysfunction activates cardiac fibroblasts and stimulates interstitial collagen deposition, increasing passive myocardial stiffness and impairing diastolic function.

3.7. Nox4TG618 mice with mitochondrial overexpression of catalase or NOX4 inhibition have reduced myocardial fibrosis and preserved diastolic function

To examine whether reduction of mtOS preserves LV diastolic function, we crossed mice with mitochondria-targeted human catalase overexpression with *Nox4*TG618 mice (*Nox4*TG618/mCAT). MitoSOX red fluorescent staining of the ventricular sections showed a significant reduction of mitochondrial superoxide generation in double transgenic mice compared with *Nox4*TG618 mice ($P < 0.0001$; Fig. 7A). Oxidative modification of the mtDNA was also significantly reduced in double-transgenic mice as demonstrated by a decreased co-localization of 8-OHdG with mitochondrial marker ATP5G2 ($P < 0.0001$; Fig. 7B). Echocardiography measurements revealed significant reduction of E/E′, left atrial volume and isovolumic relaxation time in double transgenic animals compared with *Nox4*TG618 mice ($P < 0.05$, $P < 0.01$, and $P < 0.01$, respectively; Fig. 7C, D and E). Further, ejection fraction and fractional shortening, LV end-diastolic volume and E/A were not different among *mCAT*, *Nox4*TG618/mCAT, and *Nox4*TG618 animals (Fig. 7F–I). These findings indicate normalization of LV filling pressure in *Nox4*TG618/mCAT animals and suggest that mitigating mitochondrial oxidative stress may play a critical role in the preservation of diastolic function.

In order to better understand the mechanisms that result in improved cardiac diastolic function, we also assessed cardiac fibroblast activation and the extent of interstitial fibrosis in ventricular sections of transgenic mice. Double transgenic mice showed a significantly smaller picrosirius red-positive area than *Nox4*TG618 mice ($P < 0.0001$; Fig. 7J). Furthermore, immunofluorescent staining of collagen I showed significantly less interstitial collagen deposits in double transgenic mice ($P < 0.0001$; Fig. 7K). This result is supported by the significantly reduced periostin and ACTA2 positive cells in ventricular sections of double transgenic versus *Nox4*TG618 mice ($P < 0.01$ and $P < 0.0001$, respectively; Fig. 7L and M).

A similar result was obtained when NOX4 activity was blocked in *Nox4*TG618 mice with GKT137831, a specific inhibitor of NOX1/NOX4 NADPH oxidase [29]. Baseline echocardiography and cardiac function data showed no differences in cardiac function between the genotypes in 9-month old mice prior to GKT137831 treatment (SI Appendix, Fig. S3). Wild-type mice treated with GKT137831 for 3 months showed no significant differences in cardiac function parameters compared with the vehicle control group. The treatment of *Nox4*TG618 mice led to a significant reduction in E/E′, LA volume and isovolumic relaxation time ($P < 0.05$, $P < 0.05$ and $P < 0.01$, Fig. 8A, B and C, respectively), without an effect on ejection fraction and fractional shortening, LV end-diastolic volume and E/A (Fig. 8D and E), suggesting preserved diastolic function. Similarly to the observations in the mice with mitochondrial catalase overexpression, treatment with GKT137831 reduced mitochondrial superoxide generation in *Nox4*TG618 as determined by MitoSOX Red staining ($P < 0.001$; Fig. 8H) and decreased oxidative mtDNA modification as indicated by 8-OHdG and ATP5G2 colocalization ($P < 0.01$; Fig. 8I). Additionally, inhibition of NOX4 caused significantly smaller picrosirius red-positive areas ($P < 0.001$; Fig. 8J) and less collagen I deposition in ventricular sections ($P < 0.001$; Fig. 8K) compared to vehicle-treated mice. There were significantly fewer activated fibroblasts, as reflected by periostin staining, and ACTA2-positive myofibroblasts in the sections of *Nox4*TG618 mice treated with the NOX4 inhibitor ($P < 0.0001$ and $P < 0.001$, respectively; Fig. 8L and M). Together, the data confirm that mitochondrial oxidative stress triggers DD by regulating fibrosis, and that reducing NOX4-dependent ROS levels inhibits cardiac fibroblast activation and myocardial remodeling, thereby preserving myocardial function.

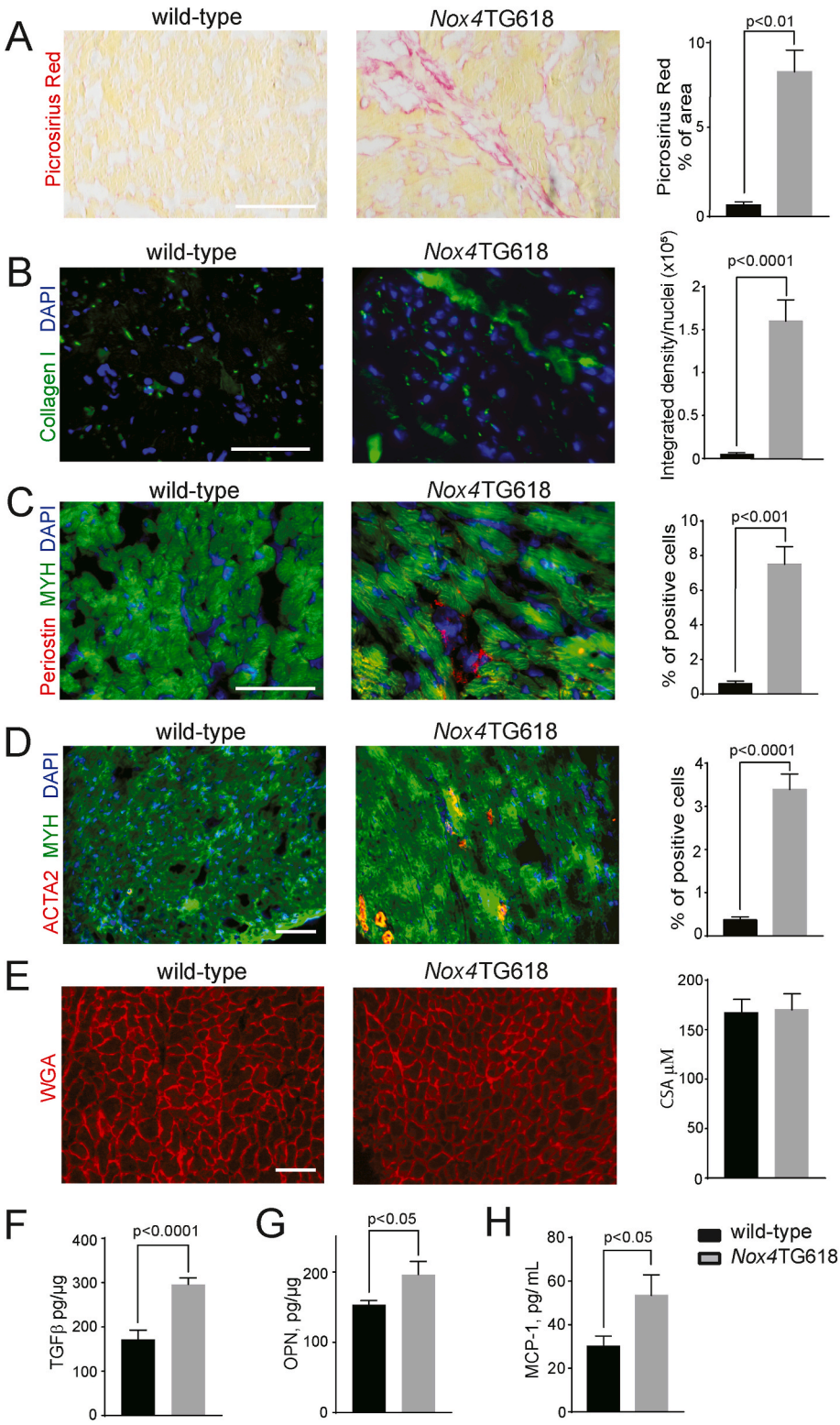

Fig. 6. Myofibroblast activation and ECM synthesis is increased in the LV of *Nox4*TG618 mice. **A)** LV fibrosis was measured by staining LV cross sections with picrosirius red (N = 9). **(B)** Immunofluorescent analysis and quantification of collagen I deposition (N = 9). Myofibroblast activation in LV cross sections was measured by immunofluorescent staining for periostin **(C)**, and ACTA2 (N = 9) **(D)**. LV cross sections were counterstained with cardiomyocyte marker MYH7. Representative images of LV cross sections stained with WGA and quantification of cardiomyocyte cross-sectional area (CSA) (N = 9) **(E)**. Concentrations of **(F)** TGFβ (N = 13) and **(G)** osteopontin (OPN, N = 7) in LV myocardium lysates, and **(H)** MCP-1 (N = 15) in mouse plasma. The data are presented as mean ± SEM. Scale is 100 µm. . (For interpretation of the references to colour in this figure legend, the reader is referred to the Web version of this article.)

3.8. Myocardial NOX4 expression and mitochondrial ROS are correlated with higher calpain levels and interstitial fibrosis in patients with diastolic dysfunction

We identified increased NOX4 expression and mitochondrial ROS in heart samples from DD patients, therefore we also analyzed the activated fibroblasts and the extent of fibrosis in those samples. Picrosirius red-positive area was significantly larger in the sections from DD patients than controls ($P < 0.05$; Fig. 9A). Immunofluorescence staining revealed collagen I deposits were greater in the DD group ($P < 0.001$; Fig. 9B). There was also a significantly higher percentage of periostin-expressing activated fibroblasts ($P < 0.05$; Fig. 9C) and ACTA2-positive myofibroblasts ($P < 0.01$; Fig. 9D) in the hearts of DD patients. LV myocardial protein lysates from the DD patients revealed similar trends in proteins involved in mitochondrial dynamics to those observed in *Nox4*TG618 mice. The expression of VDAC did not differ

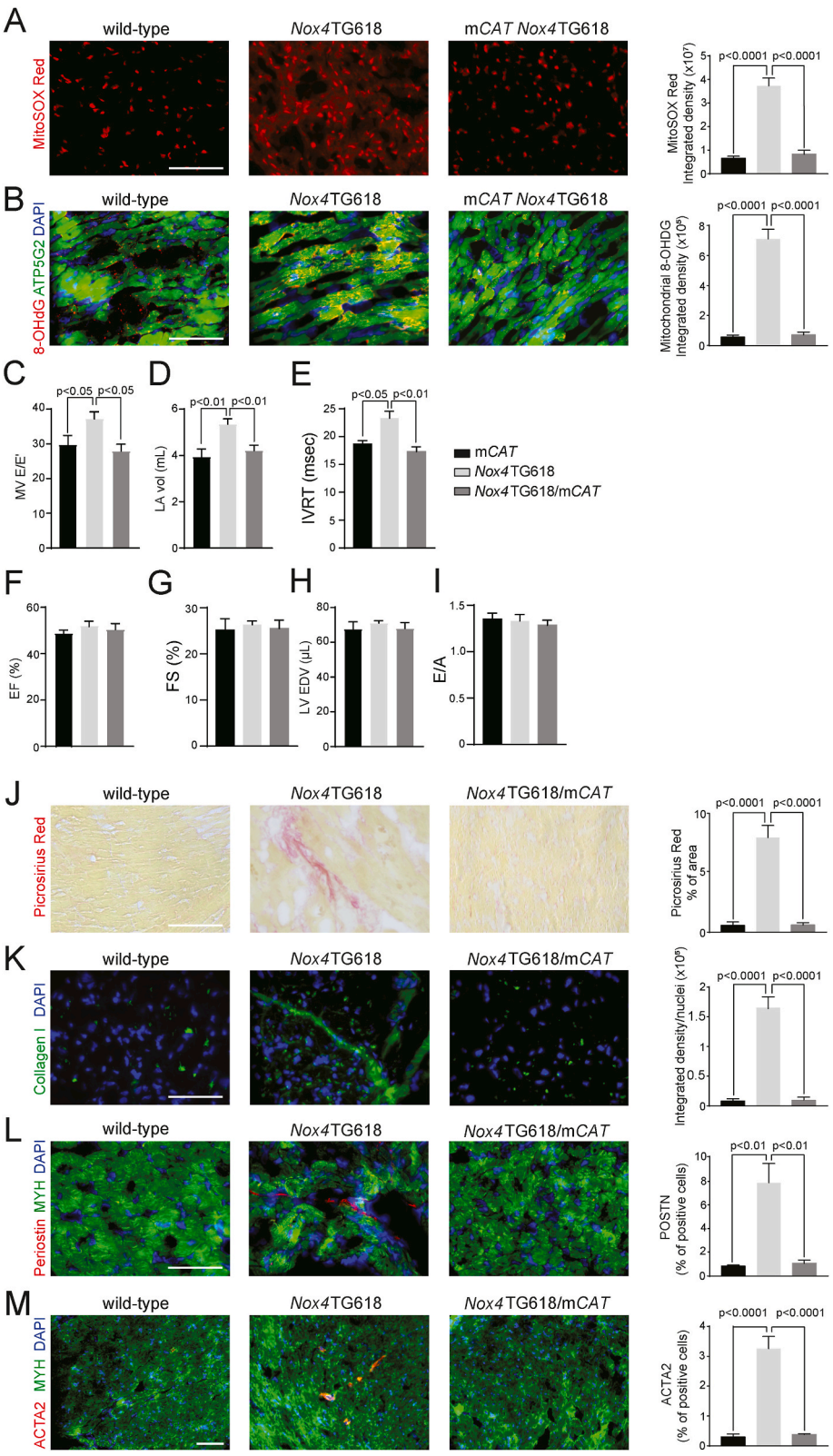

Fig. 7. Mitochondrial overexpression of human catalase inhibits mitochondrial oxidative stress, reduces activation of myofibroblasts, ECM synthesis, and preserves diastolic function in *Nox4*TG618 mice.

Representative images and quantification of **(A)** MitoSox Red and **(B)** ATP5/8-OHDG. **(C–I)** Echocardiographic assessment of systolic and diastolic function. **(C)** Ratio of MV E velocity to E′ velocity at septal annulus (E/E′), **(D)** left atrial volume (LA vol), **(E)** isovolumic relaxation time (IVRT), **(F)** ejection fraction (EF), **(G)** fractional shortening (FS), **(H)** LV end-diastolic volume (LV EDV), and **(I)** ratio of mitral valve E velocity to A velocity (E/A) (N = 7). Representative immunofluorescence images and quantification of **(J)** picrosirius red staining, **(K)** Collagen I, **(L)** periostin and **(M)** ACTA2 in mouse LV cross sections, counterstained with cardiomyocyte marker MYH (N = 7). The data are presented as mean ± SEM. Scale is 100 μm. . (For interpretation of the references to colour in this figure legend, the reader is referred to the Web version of this article.)

between the groups (Fig. 9E). Similarly, FIS1 and DRP1 protein levels were not significantly different, but DRP1 phosphorylation was significantly higher (2.2-fold, $P < 0.01$; Fig. 9E) in the protein lysates of patients with DD compared with controls. As with the *Nox4*TG618 mouse DD model, protein expression of OPA1 and MFN1 for the two patient groups were similar, whereas MFN2 expression was significantly lower in DD patients (2.1-fold, $P < 0.05$; Fig. 9F), suggesting deficits in mitochondrial turnover regulation. We examined differences in calpain system as well and our results showed that protein levels of calpain1 were not different, however, calpain 2 expression was significantly higher (2.4-fold, $P < 0.05$; Fig. 9G) in DD compared with the control group. However, protein levels of calpastatin were significantly reduced

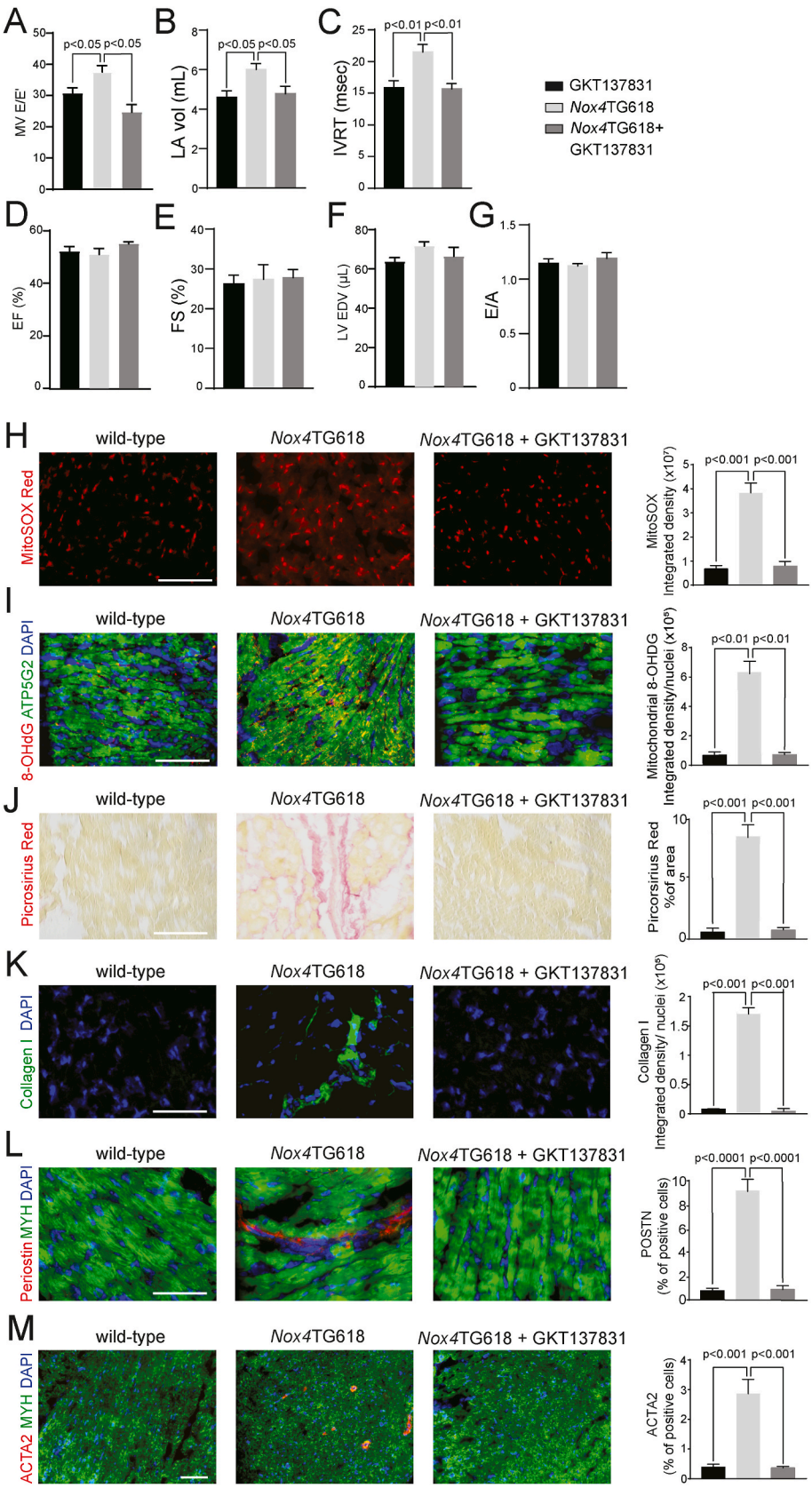

Fig. 8. Treatment with GKT137831 inhibits mitochondrial oxidative stress, decreases fibrosis and prevents development of diastolic dysfunction in *Nox4*TG618 mice.

(A–G) Echocardiographic assessment of systolic and diastolic function. **(A)** Ratio of MV E velocity to E′ velocity at septal annulus (E/E′), **(B)** left atrial volume (LA vol), (C) isovolumic relaxation time (IVRT), **(D)** ejection fraction (EF), **(E)** fractional shortening (FS), **(F)** LV end-diastolic volume (LV EDV), and **(G)** ratio of mitral valve E velocity to A velocity (E/A) (N = 7). Representative images and quantification of **(H)** MitoSox Red staining, **(I)** ATP5G2/8-OHDG colocalization, **(J)** picrosirius red staining, **(K)** collagen I, **(L)** periostin and **(M)** ACTA2 in mouse LV sections, counterstained with cardiomyocyte marker MYH (N = 7). The data are presented as mean ± SEM. Scale is 100 µm. . (For interpretation of the references to colour in this figure legend, the reader is referred to the Web version of this article.)

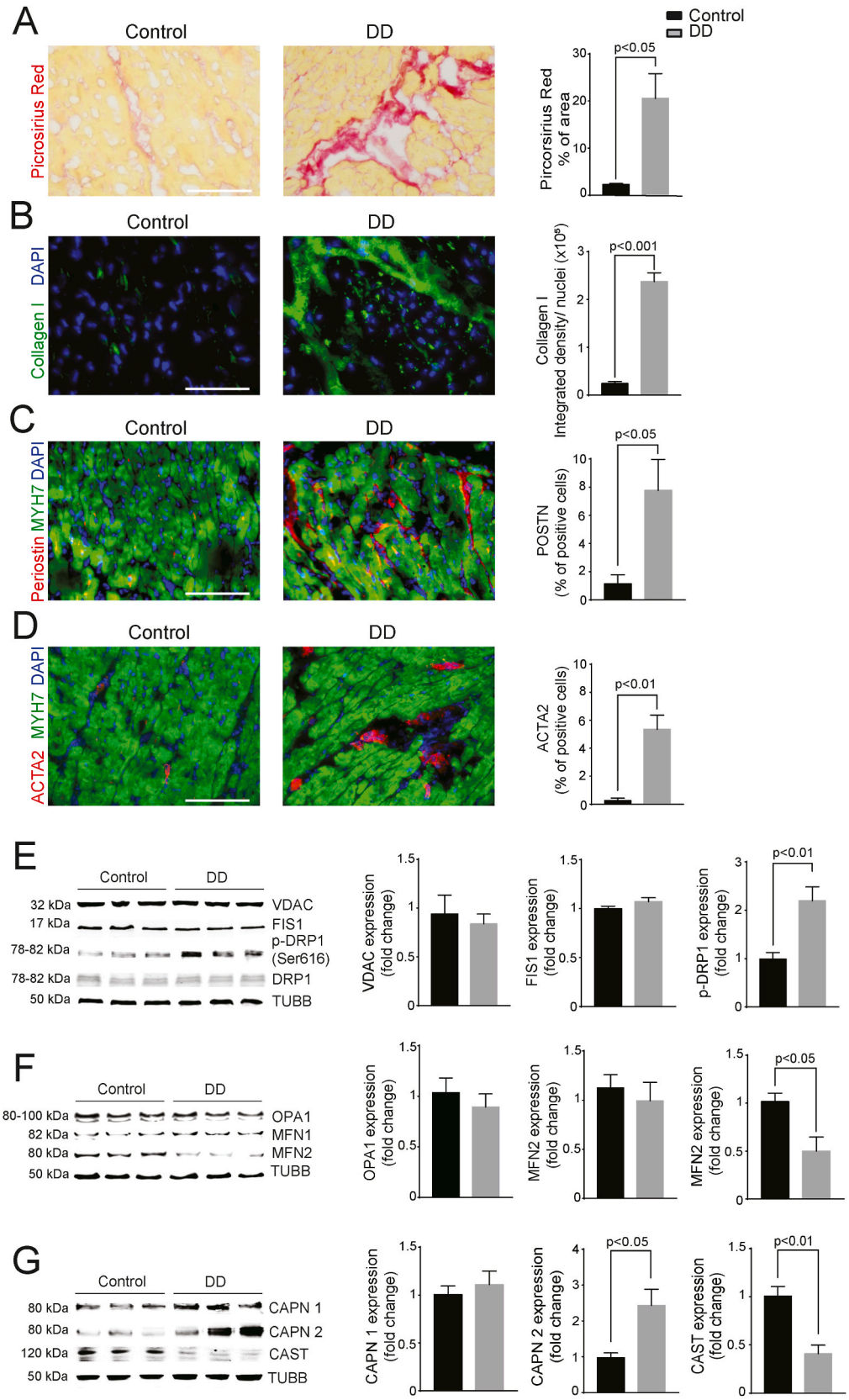

Fig. 9. LV samples of diastolic dysfunction patients show increased fibrosis and myofibroblast activation/Representative immunofluorescent images and quantification of **(A)** picrosirius red staining, **(B)** collagen I, **(C)** periostin, and **(D)** ACTA2 in human LV cross sections and counterstained for cardiomyocyte marker MYH. Western blot analysis and quantification of expression of proteins involved in mitochondrial fission **(E)**, fusion **(F),** and of calpain 1/2 (CAPN1/2) and calpastatin (CAST) **(G)** in human LV myocardial lysates. The data are presented as mean ± SEM, N = 3. Scale is 100 μm. . (For interpretation of the references to colour in this figure legend, the reader is referred to the Web version of this article.)

(2.5-fold, $P < 0.01$, Fig. 9G).

These data support the hypothesis that increased mitochondrial oxidative stress and dysfunction associated with upregulation of NOX4 expression in the heart result in less cardiac mitochondrial turnover, activation of cardiomyocyte calcium-dependent proteolytic enzymes, activation of cardiac fibroblasts, adverse matrix remodeling, and impaired diastolic function. These findings also suggest that mitochondrial targeted NOX4 overexpression in mice replicates key features of human DD.

4. Discussion

The study provides the first demonstration of excess mitochondrial ROS causing DD in mice using a transgenic mouse model of mitochondrial *Nox4* overexpression that replicates increased mitochondrial oxidative stress associated with aging, without requiring other stimuli such as high fat diet, mechanical stress, or hypertension. In addition, the NOX4 levels in our transgenic mice are similar to those in the hearts of patients with heart failure [50,51], supporting the relevance of our model for modeling human DD. Our results show that (i) middle-aged *Nox4*TG618 mice show significantly increased E/E′ ratio and elevated isovolumic relaxation time; (ii) a significant increase in left atrial volume without a significant difference in ejection fraction and LV end diastolic volume; (iii) elevated EDP and EDPVR, concordant with increased in LV diastolic myocardial stiffness and increased Tau Glantz and decreased dP/dt_{min} in pressure-volume loop analysis confirming prolonged relaxation time of the LV; (iv) increased levels of superoxide and H_2O_2 in the LV and mtDNA damage; (v) significant drop in maximal mitochondrial oxygen consumption rate and reserve respiratory capacity of cardiomyocytes, as well as lower citrate synthase and complex I activities in the LV lysates; (vi) significant reduction in mitochondrial size in the CM, in agreement with increased mitochondrial fission and impaired fusion; (vii) a marked increase in pro-fibrotic cytokine production inducing fibroblast activation and excessive ECM deposition, stiffening the LV wall; (viii) higher I_{CaL} density in ventricular CM and increased calpain 2 expression in ventricular lysates, sarcomere disarray, and increased myocardial fibrosis. NOX4-derived mitochondrial oxidative stress appears to play a mechanistic role in the pathogenesis of DD as evidenced by increased NOX4 expression levels in CM and higher myocardial mitochondrial superoxide levels, mtDNA damage, lower citrate synthase activity, greater interstitial fibrosis, impaired mitochondrial dynamics and increased calpain 2 expression in the hearts of DD patients. Further supporting the causative role of NOX4-derived mtOS in DD in our model, *Nox4*TG618/m*CAT* mice or *Nox4*TG618 mice treated with GKT137831 showed a significant reduction in interstitial fibrosis and E/E′ when compared with untreated *Nox4*TG618 mice. There is no difference in baseline echocardiographic and pressure-volume relationship data between wild-type mice and Nox4TG618 mice prior to treatment with GKT137831, indicating the treatments prevented diastolic dysfunction rather than reversed it.

Mitochondrial fusion and fission are two processes involved in maintaining mtDNA integrity and the removal of non-functional mitochondria [52]. Interestingly, mitochondrial content and oxidative capacity were abnormal, but MFN2 expression, one of the main proteins involved in mitochondrial fusion, and not MFN1 expression, was decreased in the skeletal muscle of older patients with HFpEF [53]. In line with that, we found lower levels of MFN2 in the hearts of *Nox4* transgenic mice, suggesting a reduced level of mitochondrial fusion. Furthermore, *Nox4*TG618 hearts show enhanced mitochondrial fission because DRP1 phosphorylation is significantly increased, while mitophagy is unaffected. Similarly, reduced MFN2 expression and increased DRP1 phosphorylation levels in LV samples from DD patients are evidence of reduced mitochondrial size without adversely affecting overall mitochondrial density. This agrees with previously reported excessive mitochondrial fragmentation in the myocardium of HFpEF patients compared with healthy donors [54]. These results are also in line with reports showing a relationship between mitochondrial oxidative stress and mitochondrial fragmentation through activation of DRP1 [55,56]. Moreover, MFN2 expression was reduced, and the rate of cardiomyocyte apoptosis increased in following oxidative stress by Ang II [57], whereas overexpression of MFN2 in cardiomyocytes restored mitochondrial function by promoting mitofusion in diabetic cardiomyopathy [58].

Our data show significant decrease of the mitochondrial citrate synthase and complex I activities in the LV myocardium of *Nox4*TG618 mice as well as a decline in ATP-driven, maximal mitochondrial OCR and respiratory reserve capacity, suggesting reduced ability to meet cellular ATP demand due to impaired electron transport through the ETC. The mitochondrial complex I is the most vulnerable to oxidative (supercomplex) damage. It is likely that mitochondrial complex I dysfunction results in bioenergetic impairment and cardiac ADP insensitivity, resulting in ADP-induced myocardial stiffening [59,60]. The mismatch between ATP production and cellular demand itself activates molecular pathways that lead to inflammation, cardiac remodeling, and DD [23]. Intriguingly, mitochondrial dysfunction, including decreased OXPHOS, reduced ETC complexes activity, decreased ATP synthesis, as well as structural changes of the organelle have been extensively linked to cardiovascular aging [61,62]. The notion is consistent with our previous finding that increased NOX4 expression/activity is associated with cardiovascular aging [19,21,29].

Apoptosis of cardiomyocytes is associated with the local release of pro-fibrotic factors, such as TGFβ and osteopontin [63]. Increased levels of these factors activate cardiac fibroblasts and promote their differentiation into myofibroblasts in the LV of *Nox4*TG618 mice. Over time, myofibroblasts produce excess ECM, including collagen I, resulting in adverse cardiac remodeling leading to increased LV wall stiffness and subsequent changes in diastolic function. These observations confirm the results from human heart samples, in which activated fibroblasts, myofibroblasts, and an interstitial deposition of collagen I in the myocardium are prominent features of DD. One of the most common characteristics of HFpEF is elevated LV filling pressure (LVFP) which, depending on the disease stage, may increase only when the patient is stressed or exercising, or even at rest in advanced stages of the disease [64]. In agreement with that, cardiac function tests in *Nox4*TG618 compared with wild-type mice also show an elevated LVFP and increased left atria volume. In patients with HFpEF, the elevation of LVFP is related to DD, and their LV diastolic pressure-volume relationship curve is shifted up and to the left, reflecting increased passive chamber stiffness [7]. Similar findings were also observed in PV loops of *Nox4* transgenic mice. These mice have increased LV diastolic stiffness and increased filling pressure as EDP and EDPVR are elevated compared with wild-type mice. As demonstrated by the fact that mitochondrial SOD mimetic and selective NOX1/4 inhibitor prevented excessive fibrosis and preserved diastolic function in *Nox4*TG618 mice, fibrosis may be the primary factor for LV stiffness and DD. It should also be noted that arterial stiffening is an important factor in left ventricular DD [65]. Aortic stiffness is increased in *Nox4* transgenic mice [21], whereas proximal aortic stiffness is associated with the development of HFpEF in patients with asymptomatic DD [66].

Another potential cause of LV stiffness and impaired LV filling may be the changes in the Z-disk structure that we observed in *Nox4*TG618 mice. The degradation of cardiomyocyte Z-disks in transgenic mice might be explained by an increase in calpain 2 expression/activity. SMN complex is colocalized to Z-disks and performs a muscle-specific function, this complex is also a target for direct proteolysis by calpains [67]. In addition, calpains proteolyze the spring-like domain of titin, which may predispose cardiomyocytes to DD [68]. Several lines of evidence indicate a connection between oxidative stress and calpain activation, both directly and indirectly. The intracellular concentration of free Ca^{2+} plays a critical role in excitation-contraction coupling in cardiomyocytes, and LTCC is the primary entry point of Ca^{2+} [42]. In addition, there is a critical crosstalk between ROS and Ca^{2+} in

cardiomyocytes, and Ca^{2+} overload causes mitochondrial dysfunction and cell death [69]. LTCC cysteine residues were oxidatively modified by H_2O_2, increasing the Ca^{2+} current [70]. Cellular redox state also regulates intracellular Ca^{2+} overload by affecting the function of LTCC [71], suggesting LTCC is the main regulator of Ca^{2+} homeostasis in cardiomyocytes under oxidative stress conditions and may be involved in pathological remodeling of the heart.

Zeng et al. have shown that superoxide activates LTCCs in rat cardiomyocytes via a PKC-dependent mechanism [72]. Additionally, H_2O_2 has been shown to increase the L-type Ca^{2+} current in ventricular cardiomyocytes [73]. The increased Ca^{2+} uptake in cardiomyocytes during oxidative stress impacted mitochondrial ROS production, resulting in a persistent increase in open probability of the channel and an increase in Ca^{2+} influx [42]. The data support our observation that LTCC activation is increased in transgenic mice and suggests that this is a potential contributor to mitochondrial dysfunction which can also exacerbate mitochondrial oxidative stress. Moreover, Ca^{2+} influx via LTCC activates calpains. This is supported by the observation that oxidative stress leads to increased Ca^{2+} influx and upregulation of calpain in PC12 cells [74]. In contrast, genetic deletion of $Ca_v1.4$ L-type voltage-gated calcium channels inhibits calpain, reducing apoptosis in photoreceptors of mice with retinitis pigmentosa [45].

The intracellular Ca^{2+} dynamics in cardiomyocytes are affected by impaired mitochondrial function, cellular oxidative stress, and increased Ca^{2+} influx. Increased mtROS production causes mitochondria in the neighboring cell to release more ROS, a process called "ROS-induced ROS release" that results in activation of a redox signaling cellular network resulting in dysregulation of excitation-contraction coupling [75]. Oxidative stress increases calcium ion concentration by elevating LTCC current [76], while oxidative modification of Ca^{2+}/calmodulin-dependent protein kinase II (CaMKII) leads to its activation [77], and subsequent LTCC phosphorylation and increased calcium uptake. Therefore, the results obtained in *Nox4*TG618 mice of hyperactive LTCC in cardiomyocytes in combination with increased IVRT, Tau Glantz, and dP/dTmin suggest that mitochondrial dysfunction results in inadequate relaxation of the LV and reduced diastolic function. This is in agreements with reports indicating that diastolic Ca^{2+} overload negatively affects cardiomyocyte relaxation and hence, cardiac diastolic function in the human heart [78–81].

Study limitations: Our mitochondrial-targeted Nox4 overexpression mouse model replicated an increase in mitochondrial oxidative stress associated with aging at a relatively early age. The *Nox4*TG618 mice also have impaired aortic compliance, and the model closely mimics the development of diastolic dysfunction in humans. Yet there are several limitations to the model. Diastolic dysfunction in this model results from direct genetic manipulation. Other risk factors for diastolic dysfunction such as hypertension, coronary artery disease, diabetes, and increased body mass index are not phenocopied by the model. Therefore, there is uncertainty whether the pathophysiological mechanisms elucidated in this model adequately explain the human onset of DD. Our study was also limited by a rather small sample size of human LVs, which prevented us from conducting association studies.

In summary, we demonstrate that increased mitochondrial NOX4 expression causes DD in mice. Essentially, increased H_2O_2 production in the cardiomyocyte mitochondria leads to oxidative damage of mitochondrial DNA and promotes mitochondrial dysfunction, which, combined with dysregulated mitochondrial dynamics, leads to increased cardiomyocyte apoptosis. This together with increased synthesis of pro-inflammatory and pro-fibrotic cytokines in LV myocardium, activation of fibroblasts, and accumulation of extracellular matrix leads to interstitial fibrosis and passive stiffness of the myocardium. Additionally, mitochondrial dysfunction and dysregulated Ca^{2+} dynamics adversely influence myocardial relaxation, compliance, and filling pressure. The fact that NOX4-dependent mitochondrial ROS inhibited cardiac fibrosis and preserved diastolic function makes therapeutic strategies that enhance mitochondrial function a potentially beneficial approach in at risk individuals to ameliorate the progression to HFpEF.

Conflict of interest

Dr. Marschall Runge is a member of the Board of Directors at Eli Lilly and Company.

Appendix A. Supplementary data

Supplementary data to this article can be found online at https://doi.org/10.1016/j.redox.2022.102474.

References

[1] M.A. Pfeffer, A.M. Shah, B.A. Borlaug, Heart failure with preserved ejection fraction in perspective, Circ. Res. 124 (2019) 1598–1617.
[2] R.J. Desai, M. Mahesri, K. Chin, R. Levin, R. Lahoz, R. Studer, M. Vaduganathan, E. Patorno, Epidemiologic characterization of heart failure with reduced or preserved ejection fraction populations identified using medicare claims, Am. J. Med. 134 (2021) e241–e251.
[3] M.S. Loop, M.K. Van Dyke, L.G. Chen, T.M. Brown, R.W. Durant, M.M. Safford, E. B. Levitan, Comparison of length of stay, 30-day mortality, and 30-day readmission rates in medicare patients with heart failure and with reduced versus preserved ejection fraction, Am. J. Cardiol. 118 (2016) 79–85.
[4] S.M. Dunlay, V.L. Roger, M.M. Redfield, Epidemiology of heart failure with preserved ejection fraction, Nat. Rev. Cardiol. 14 (2017) 591–602.
[5] S.J. Shah, D.H. Katz, S. Selvaraj, M.A. Burke, C.W. Yancy, M. Gheorghiade, R. O. Bonow, C.C. Huang, R.C. Deo, Phenomapping for novel classification of heart failure with preserved ejection fraction, Circulation 131 (2015) 269–279.
[6] S.D. Anker, J. Butler, G. Filippatos, J.P. Ferreira, E. Bocchi, M. Bohm, H.P. Brunner-La Rocca, D.J. Choi, V. Chopra, E. Chuquiure-Valenzuela, N. Giannetti, J.E. Gomez-Mesa, S. Janssens, J.L. Januzzi, J.R. Gonzalez-Juanatey, B. Merkely, S.J. Nicholls, S.V. Perrone, I.L. Pina, P. Ponikowski, M. Senni, D. Sim, J. Spinar, I. Squire, S. Taddei, H. Tsutsui, S. Verma, D. Vinereanu, J. Zhang, P. Carson, C.S.P. Lam, N. Marx, C. Zeller, N. Sattar, W. Jamal, S. Schnaidt, J.M. Schnee, M. Brueckmann, S.J. Pocock, F. Zannad, M. Packer, E.M.-P.T. Investigators, Empagliflozin in heart failure with a preserved ejection fraction, N. Engl. J. Med. 385 (2021) 1451–1461.
[7] D. Westermann, M. Kasner, P. Steendijk, F. Spillmann, A. Riad, K. Weitmann, W. Hoffmann, W. Poller, M. Pauschinger, H.P. Schultheiss, C. Tschope, Role of left ventricular stiffness in heart failure with normal ejection fraction, Circulation 117 (2008) 2051–2060.
[8] B.A. Borlaug, W.J. Paulus, Heart failure with preserved ejection fraction: pathophysiology, diagnosis, and treatment, Eur. Heart J. 32 (2011) 670–679.
[9] B. Yang, D.F. Larson, J. Ranger-Moore, Biphasic change of tau (tau) in mice as arterial load acutely increased with phenylephrine injection, PLoS One 8 (2013), e60580.
[10] A.M. Shah, S.J. Shah, I.S. Anand, N.K. Sweitzer, E. O'Meara, J.F. Heitner, G. Sopko, G. Li, S.F. Assmann, S.M. McKinlay, B. Pitt, M.A. Pfeffer, S.D. Solomon, T. Investigators, Cardiac structure and function in heart failure with preserved ejection fraction: baseline findings from the echocardiographic study of the Treatment of Preserved Cardiac Function Heart Failure with an Aldosterone Antagonist trial, Circ Heart Fail 7 (2014) 104–115.
[11] G.C. Kane, B.L. Karon, D.W. Mahoney, M.M. Redfield, V.L. Roger, J.C. Burnett Jr., S.J. Jacobsen, R.J. Rodeheffer, Progression of left ventricular diastolic dysfunction and risk of heart failure, JAMA 306 (2011) 856–863.
[12] C. Maack, M. Bohm, Targeting mitochondrial oxidative stress in heart failure throttling the afterburner, J. Am. Coll. Cardiol. 58 (2011) 83–86.
[13] D.F. Dai, S.C. Johnson, J.J. Villarin, M.T. Chin, M. Nieves-Cintron, T. Chen, D. J. Marcinek, G.W. Dorn 2nd, Y.J. Kang, T.A. Prolla, L.F. Santana, P.S. Rabinovitch, Mitochondrial oxidative stress mediates angiotensin II-induced cardiac hypertrophy and Galphaq overexpression-induced heart failure, Circ. Res. 108 (2011) 837–846.
[14] O. Sorop, I. Heinonen, M. van Kranenburg, J. van de Wouw, V.J. de Beer, I.T. N. Nguyen, Y. Octavia, R.W.B. van Duin, K. Stam, R.J. van Geuns, P.A. Wielopolski, G.P. Krestin, A.H. van den Meiracker, R. Verjans, M. van Bilsen, A.H.J. Danser, W. J. Paulus, C. Cheng, W.A. Linke, J.A. Joles, M.C. Verhaar, J. van der Velden, D. Merkus, D.J. Duncker, Multiple common comorbidities produce left ventricular diastolic dysfunction associated with coronary microvascular dysfunction, oxidative stress, and myocardial stiffening, Cardiovasc. Res. 114 (2018) 954–964.
[15] M. Raad, A. AlBadri, J. Wei, P.K. Mehta, J. Maughan, A. Gadh, L. Thomson, D. P. Jones, A.A. Quyyumi, C.J. Pepine, C.N.B. Merz, Oxidative stress is associated with diastolic dysfunction in women with ischemia with no obstructive coronary artery disease, J. Am. Heart Assoc. 9 (2020).
[16] T. Ago, S. Matsushima, J. Kuroda, D. Zablocki, T. Kitazono, J. Sadoshima, The NADPH oxidase Nox4 and aging in the heart, Aging (Albany NY) 2 (2010) 1012–1016.
[17] J. Kuroda, T. Ago, S. Matsushima, P.Y. Zhai, M.D. Schneider, J. Sadoshima, NADPH oxidase 4 (Nox4) is a major source of oxidative stress in the failing heart, Proc. Natl. Acad. Sci. U.S.A. 107 (2010) 15565–15570.
[18] M.D. Stevenson, C. Canugovi, A.E. Vendrov, T. Hayami, D.E. Bowles, K.H. Krause, N.R. Madamanchi, M.S. Runge, NADPH oxidase 4 regulates inflammation in

ischemic heart failure: role of soluble epoxide hydrolase, Antioxidants Redox Signal. 31 (2019) 39–58.
[19] E.M. Jeong, J. Chung, H. Liu, Y. Go, S. Gladstein, A. Farzaneh-Far, E. D. Lewandowski, S.C. Dudley Jr., Role of mitochondrial oxidative stress in glucose tolerance, insulin resistance, and cardiac diastolic dysfunction, J. Am. Heart Assoc. 5 (2016).
[20] A. Lozhkin, A.E. Vendrov, H. Pan, S.A. Wickline, N.R. Madamanchi, M.S. Runge, NADPH oxidase 4 regulates vascular inflammation in aging and atherosclerosis, J. Mol. Cell. Cardiol. 102 (2017) 10–21.
[21] C. Canugovi, M.D. Stevenson, A.E. Vendrov, T. Hayami, J. Robidoux, H. Xiao, Y. Y. Zhang, D.T. Eitzman, M.S. Runge, N.R. Madamanchi, Increased mitochondrial NADPH oxidase 4 (NOX4) expression in aging is a causative factor in aortic stiffening, Redox Biol. 26 (2019), 101288.
[22] H.L. Kim, W.H. Lim, J.B. Seo, W.Y. Chung, S.H. Kim, M.A. Kim, J.H. Zo, Association between arterial stiffness and left ventricular diastolic function in relation to gender and age, Medicine 96 (2017).
[23] A.A. Kumar, D.P. Kelly, J.A. Chirinos, Mitochondrial dysfunction in heart failure with preserved ejection fraction, Circulation 139 (2019) 1435–1450.
[24] D.F. Dai, T. Chen, H. Szeto, M. Nieves-Cintron, V. Kutyavin, L.F. Santana, P. S. Rabinovitch, Mitochondrial targeted antioxidant Peptide ameliorates hypertensive cardiomyopathy, J. Am. Coll. Cardiol. 58 (2011) 73–82.
[25] M.T. Waddingham, T. Sonobe, H. Tsuchimochi, A.J. Edgley, V. Sukumaran, Y. C. Chen, S.S. Hansra, D.O. Schwenke, K. Umetani, K. Aoyama, N. Yagi, D.J. Kelly, S. Gaderih, M. Herwig, D. Kolijn, A. Mugge, W.J. Paulus, T. Ogo, M. Shirai, N. Hamdani, J.T. Pearson, Diastolic dysfunction is initiated by cardiomyocyte impairment ahead of endothelial dysfunction due to increased oxidative stress and inflammation in an experimental prediabetes model, J. Mol. Cell. Cardiol. 137 (2019) 119–131.
[26] I. Rabinovich-Nikitin, R. Dhingra, L.A. Kirshenbaum, Activation of mitophagy in high-fat diet-induced diabetic cardiomyopathy, Circ. Res. 124 (2019) 1288–1290.
[27] M.M. Tong, T. Saito, P.Y. Zhai, S. Oka, W. Mizushima, M. Nakamura, S. Ikeda, A. Shirakabe, J. Sadoshima, Mitophagy is essential for maintaining cardiac function during high fat diet-induced diabetic cardiomyopathy, Circ. Res. 124 (2019) 1360–1371.
[28] K. Block, Y. Gorin, H.E. Abboud, Subcellular localization of Nox4 and regulation in diabetes, Proc. Natl. Acad. Sci. U. S. A. 106 (2009) 14385–14390.
[29] A.E. Vendrov, K.C. Vendrov, A. Smith, J.L. Yuan, A. Sumida, J. Robidoux, M. S. Runge, N.R. Madamanchi, Nox4 NADPH oxidase-dependent mitochondrial oxidative stress in aging-associated cardiovascular disease, Antioxidants Redox Signal. 23 (2015) 1389–1409.
[30] A.L. Reed, A. Tanaka, D. Sorescu, H. Liu, E.M. Jeong, M. Sturdy, E.R. Walp, S. C. Dudley Jr., R.L. Sutliff, Diastolic dysfunction is associated with cardiac fibrosis in the senescence-accelerated mouse, Am. J. Physiol. Heart Circ. Physiol. 301 (2011) H824–H831.
[31] S. Larsen, J. Nielsen, C.N. Hansen, L.B. Nielsen, F. Wibrand, N. Stride, H. D. Schroder, R. Boushel, J.W. Helge, F. Dela, M. Hey-Mogensen, Biomarkers of mitochondrial content in skeletal muscle of healthy young human subjects, J. Physiol. 590 (2012) 3349–3360.
[32] T. Ago, J. Kuroda, J. Pain, C. Fu, H. Li, J. Sadoshima, Upregulation of Nox4 by hypertrophic stimuli promotes apoptosis and mitochondrial dysfunction in cardiac myocytes, Circ. Res. 106 (2010) 1253–1264.
[33] O.H. Cingolani, D.A. Kass, Pressure-volume relation analysis of mouse ventricular function, Am. J. Physiol. Heart Circ. Physiol. 301 (2011) H2198–H2206.
[34] T. Ide, H. Tsutsui, S. Hayashidani, D. Kang, N. Suematsu, K. Nakamura, H. Utsumi, N. Hamasaki, A. Takeshita, Mitochondrial DNA damage and dysfunction associated with oxidative stress in failing hearts after myocardial infarction, Circ. Res. 88 (2001) 529–535.
[35] P. Yue, S. Jing, L. Liu, F. Ma, Y. Zhang, C. Wang, H. Duan, K. Zhou, Y. Hua, G. Wu, Y. Li, Association between mitochondrial DNA copy number and cardiovascular disease: current evidence based on a systematic review and meta-analysis, PLoS One 13 (11) (2018), e0206003.
[36] G. Chieffi Baccari, S. Falvo, M.M. Di Fiore, F. Cioffi, A. Giacco, A. Santillo, High-fat diet affects autophagy and mitochondrial compartment in rat Harderian gland, J Exp Zool A Ecol Integr Physiol (2022 Aug 4), https://doi.org/10.1002/jez.2646.
[37] E.P.K. Yu, J. Reinhold, H. Yu, L. Starks, A.K. Uryga, K. Foote, A. Finigan, N. Figg, Y. F. Pung, A. Logan, M.P. Murphy, M. Bennett, Mitochondrial respiration is reduced in atherosclerosis, promoting necrotic core formation and reducing relative fibrous cap thickness, Arterioscler. Thromb. Vasc. Biol. 37 (2017) 2322–2332.
[38] A.M. van der Bliek, Q. Shen, S. Kawajiri, Mechanisms of mitochondrial fission and fusion, Cold Spring Harbor Perspect. Biol. 5 (6) (2013) a011072.
[39] D.A. Kubli, A.B. Gustafsson, Mitochondria and mitophagy: the yin and yang of cell death control, Circ. Res. 111 (2012) 1208–1221.
[40] B. Westermann, Mitochondrial fusion and fission in cell life and death, Nat. Rev. Mol. Cell Biol. 11 (2010) 872–884.
[41] D.F. Suen, K.L. Norris, R.J. Youle, Mitochondrial dynamics and apoptosis, Genes Dev. 22 (2008) 1577–1590.
[42] V.P. Johnstone, L.C. Hool, Glutathionylation of the L-type Ca2+ channel in oxidative stress-induced pathology of the heart, Int. J. Mol. Sci. 15 (2014) 19203–19225.
[43] C. Satpathy, T.K. Mishra, R. Satpathy, H.K. Satpathy, E. Barone, Diagnosis and management of diastolic dysfunction and heart failure, Am. Fam. Physician 73 (2006) 841–846.
[44] H.M. Viola, L.C. Hool, The L-type Ca2+ channel: a mediator of hypertrophic cardiomyopathy, Channels 11 (2017) 5–7.
[45] C. Schon, F. Paquet-Durand, S. Michalakis, Cav1.4 l-type calcium channels contribute to calpain activation in degenerating photoreceptors of rd1 mice, PLoS One 11 (2016), e0156974.
[46] K. Sharma, D.A. Kass, Heart failure with preserved ejection fraction: mechanisms, clinical features, and therapies, Circ. Res. 115 (2014) 79–96.
[47] M. Hulsmans, H.B. Sager, J.D. Roh, M. Valero-Munoz, N.E. Houstis, Y. Iwamoto, Y. Sun, R.M. Wilson, G. Wojtkiewicz, B. Tricot, M.T. Osborne, J. Hung, C. Vinegoni, K. Naxerova, D.E. Sosnovik, M.R. Zile, A.D. Bradshaw, R. Liao, A. Tawakol, R. Weissleder, A. Rosenzweig, F.K. Swirski, F. Sam, M. Nahrendorf, Cardiac macrophages promote diastolic dysfunction, J. Exp. Med. 215 (2018) 423–440.
[48] Z.V. Varga, M. Pipicz, J.A. Baán, T. Baranyai, G. Koncsos, P. Leszek, M. Kuśmierczyk, F. Sánchez-Cabo, P. García-Pavía, G.J. Brenner, Z. Giricz, T. Csont, L. Mendler, E. Lara-Pezzi, P. Pacher, P. Ferdinandy, Alternative splicing of NOX4 in the failing human heart, Front. Physiol. 8 (2017) 935.
[49] G.J. Zhao, C.L. Zhao, S. Ouyang, K.Q. Deng, L. Zhu, A.C. Montezano, C. Zhang, F. Hu, X.Y. Zhu, S. Tian, X. Liu, Y.X. Ji, P. Zhang, X.J. Zhang, Z.G. She, R.M. Touyz, H. Li, Ca^{2+}-Dependent NOX5 (NADPH Oxidase 5) exaggerates cardiac hypertrophy through reactive oxygen species production, Hypertension 76 (2020) 827–838.
[50] M. Scatena, L. Liaw, C.M. Giachelli, Osteopontin: a multifunctional molecule regulating chronic inflammation and vascular disease, Arterioscler. Thromb. Vasc. Biol. 27 (2007) 2302–2309.
[51] A. Willeford, T. Suetomi, A. Nickle, H.M. Hoffman, S. Miyamoto, J. Heller Brown, CaMKIIδ-mediated inflammatory gene expression and inflammasome activation in cardiomyocytes initiate inflammation and induce fibrosis, JCI Insight 3 (2018), e97054.
[52] H.N. Sabbah, Targeting mitochondrial dysfunction in the treatment of heart failure, Expert Rev. Cardiovasc Ther. 14 (2016) 1305–1313.
[53] A.J.A. Molina, M.S. Bharadwaj, C. Van Horn, B.J. Nicklas, M.F. Lyles, J. Eggebeen, M.J. Haykowsky, P.H. Brubaker, D.W. Kitzman, Skeletal muscle mitochondrial content, oxidative capacity, and mfn2 expression are reduced in older patients with heart failure and preserved ejection fraction and are related to exercise intolerance, Jacc-Heart Fail 4 (2016) 636–645.
[54] A.H. Chaanine, L.D. Joyce, J.M. Stulak, S. Maltais, D.L. Joyce, J.A. Dearani, K. Klaus, K.S. Nair, R.J. Hajjar, M.M. Redfield, Mitochondrial morphology, dynamics, and function in human pressure overload or ischemic heart disease with preserved or reduced ejection fraction, Circ Heart Fail 12 (2019), e005131.
[55] S. Wu, F. Zhou, Z. Zhang, D. Xing, Mitochondrial oxidative stress causes mitochondrial fragmentation via differential modulation of mitochondrial fission-fusion proteins, FEBS J. 278 (2011) 941–954.
[56] C.S. Brand, V.P. Tan, J.H. Brown, S. Miyamoto, RhoA regulates Drp1 mediated mitochondrial fission through ROCK to protect cardiomyocytes, Cell. Signal. 50 (2018) 48–57.
[57] W. Xiong, Z. Ma, D. An, Z. Liu, W. Cai, Y. Bai, Q. Zhan, W. Lai, Q. Zeng, H. Ren, D. Xu, Mitofusin 2 participates in mitophagy and mitochondrial fusion against angiotensin ii-induced cardiomyocyte injury, Front. Physiol. 10 (2019) 411.
[58] L. Hu, M.G. Ding, D.S. Tang, E.H. Gao, C.Y. Li, K.Y. Wang, B.C. Qi, J.H. Qiu, H. S. Zhao, P. Chang, F. Fu, Y. Li, Targeting mitochondrial dynamics by regulating Mfn2 for therapeutic intervention in diabetic cardiomyopathy, Theranostics 9 (2019) 3687–3706.
[59] V. Sequeira, A. Najafi, M. McConnell, E.D. Fowler, I.A. Bollen, R.C. Wüst, C. dos Remedios, M. Helmes, E. White, G.J. Stienen, J. Tardiff, D.W. Kuster, J. van der Velden, Synergistic role of ADP and Ca(2+) in diastolic myocardial stiffness, J. Physiol. 593 (2015) 3899–3916.
[60] I. Heinonen, O. Sorop, B.M. van Dalen, R.C.I. Wüst, J. van de Wouw, V.J. de Beer, Y. Octavia, R.W.B. van Duin, Y. Hoogstrate, L. Blonden, M. Alkio, K. Anttila, A. Stubbs, J. van der Velden, D. Merkus, D.J. Duncker, Cellular, mitochondrial and molecular alterations associate with early left ventricular diastolic dysfunction in a porcine model of diabetic metabolic derangement, Sci. Rep. 10 (1) (2020), 13173.
[61] A. Tocchi, E.K. Quarles, N. Basisty, L. Gitari, P.S. Rabinovitch, Mitochondrial dysfunction in cardiac aging, Biochim. Biophys. Acta 1847 (2015) 1424–1433.
[62] C.L. Hoppel, E.J. Lesnefsky, Q. Chen, B. Tandler, Mitochondrial dysfunction in cardiovascular aging, Adv. Exp. Med. Biol. 982 (2017) 451–464.
[63] Y. Lenga, A. Koh, A.S. Perera, C.A. McCulloch, J. Sodek, R. Zohar, Osteopontin expression is required for myofibroblast differentiation, Circ. Res. 102 (2008) 319–327.
[64] Y.N.V. Reddy, T.P. Olson, M. Obokata, V. Melenovsky, B.A. Borlaug, Hemodynamic correlates and diagnostic role of cardiopulmonary exercise testing in heart failure with preserved ejection fraction, JACC Heart Fail 6 (2018) 665–675.
[65] M. Mika, H. Kanzaki, T. Hasegawa, H. Fukuda, M. Amaki, J. Kim, M. Asakura, H. Asanuma, M. Nishimura, M. Kitakaze, Arterial stiffening is a crucial factor for left ventricular diastolic dysfunction in a community-based normotensive population, Int J Cardiol Hyper 6 (2020).
[66] I. Karagodin, O. Aba-Omer, R. Sparapani, J.L. Strande, Aortic stiffening precedes onset of heart failure with preserved ejection fraction in patients with asymptomatic diastolic dysfunction, BMC Cardiovasc. Disord. 17 (2017) 62.
[67] M.P. Walker, T.K. Rajendra, L. Saieva, J.L. Fuentes, L. Pellizzoni, A.G. Matera, SMN complex localizes to the sarcomeric Z-disc and is a proteolytic target of calpain, Hum. Mol. Genet. 17 (2008) 3399–3410.
[68] C.C. Lim, C. Zuppinger, X.X. Guo, G.M. Kuster, M. Helmes, H.M. Eppenberger, T. M. Suter, R.L. Liao, D.B. Sawyer, Anthracyclines induce calpain-dependent titin proteolysis and necrosis in cardiomyocytes, J. Biol. Chem. 279 (2004) 8290–8299.
[69] R.F. Feissner, J. Skalska, W.E. Gaum, S.S. Sheu, Crosstalk signaling between mitochondrial Ca2+ and ROS, Front Biosci-Landmrk. 14 (2009) 1197–1218.
[70] H.M. Viola, P.G. Arthur, L.C. Hool, Transient exposure to hydrogen peroxide causes an increase in mitochondria-derived superoxide as a result of sustained alteration

in L-type Ca2+ channel function in the absence of apoptosis in ventricular myocytes, Circ. Res. 100 (2007) 1036–1044.
[71] H.M. Viola, P.G. Arthur, L.C. Hool, Evidence for regulation of mitochondrial function by the L-type Ca2+ channel in ventricular myocytes, J. Mol. Cell. Cardiol. 46 (2009) 1016–1026.
[72] Q. Zeng, Y. Han, Y. Bao, W. Li, X. Li, X. Shen, X. Wang, F. Yao, S.T. O'Rourke, C. Sun, 20-HETE increases NADPH oxidase-derived ROS production and stimulates the L-type Ca2+ channel via a PKC-dependent mechanism in cardiomyocytes, Am. J. Physiol. Heart Circ. Physiol. 299 (2010) H1109–H1117.
[73] L. Yang, J. Xu, E. Minobe, L. Yu, R. Feng, A. Kameyama, K. Yazawa, M. Kameyama, Mechanisms underlying the modulation of L-type Ca2+ channel by hydrogen peroxide in Guinea pig ventricular myocytes, J. Physiol. Sci. 63 (2013) 419–426.
[74] S.K. Ray, M. Fidan, M.W. Nowak, G.G. Wilford, E.L. Hogan, N.L. Banik, Oxidative stress and Ca^{2+} influx upregulate calpain and induce apoptosis in PC12 cells, Brain Res. 852 (2000) 326–334.
[75] E. Bertero, C. Maack, Calcium signaling and reactive oxygen species in mitochondria, Circ. Res. 122 (2018) 1460–1478.
[76] N. Zhao, Q. Li, H. Sui, H. Zhang, Role of oxidation-dependent camkii activation in the genesis of abnormal action potentials in atrial cardiomyocytes: a simulation study, 2020, BioMed Res. Int. (2020), 1597012.
[77] Q. Wang, A.P. Quick, S. Cao, J. Reynolds, D.Y. Chiang, D. Beavers, N. Li, G. Wang, G.G. Rodney, M.E. Anderson, X.H.T. Wehrens, Oxidized CamkII ($ca^{(2+)}$/calmodulin-dependent protein kinase II) is essential for ventricular arrhythmia in a mouse model of duchenne muscular dystrophy, Circ Arrhythm Electrophysiol 11 (2018), e005682.
[78] D.A. Eisner, J.L. Caldwell, A.W. Trafford, D.C. Hutchings, The control of diastolic calcium in the heart basic mechanisms and functional implications, Circ. Res. 126 (2020) 395–412.
[79] M. Periasamy, P.M. Janssen, Molecular basis of diastolic dysfunction, Heart Fail. Clin. 4 (2008) 13–21.
[80] L. Belardinelli, J.C. Shryock, H. Fraser, The mechanism of ranolazine action to reduce ischemia-induced diastolic dysfunction, Eur. Heart J. Suppl. 8 (2006) A10–A13.
[81] L. Mandinov, F.R. Eberli, C. Seiler, O.M. Hess, Diastolic heart failure, Cardiovasc. Res. 45 (2000) 813–825.